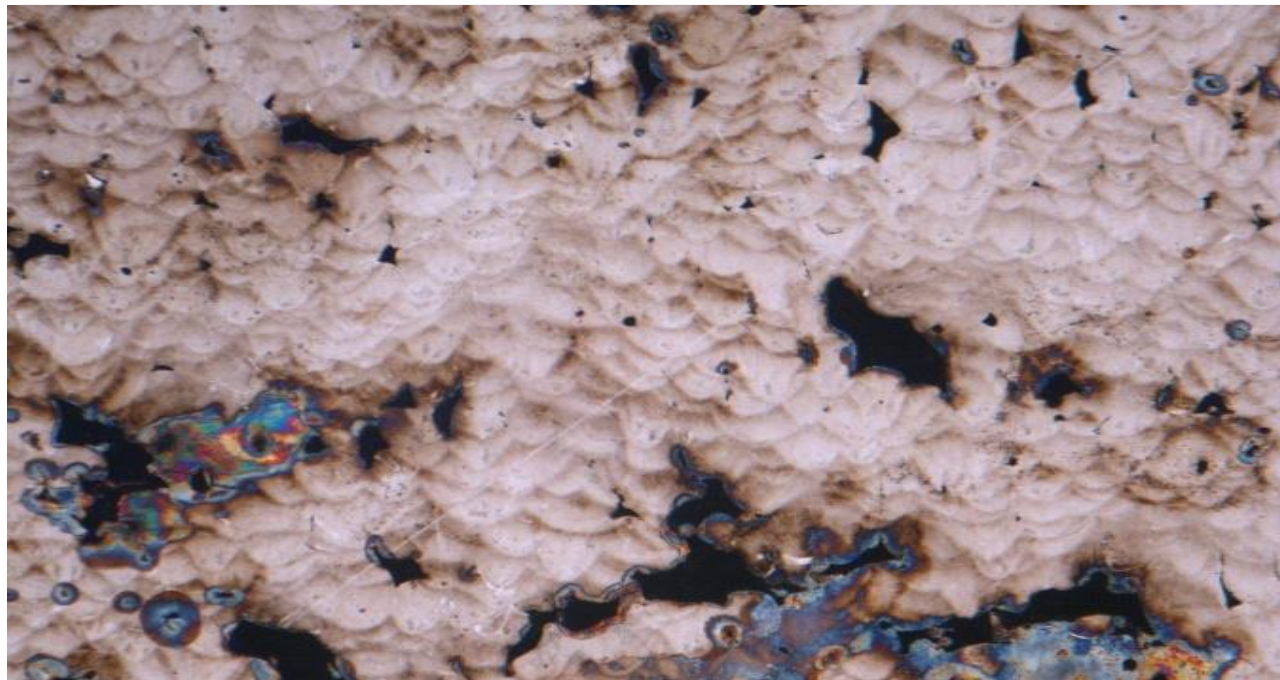




**CHALMERS**  
UNIVERSITY OF TECHNOLOGY



# Process Optimization of Additive Manufacturing of Tool Steels

Master's Thesis in Materials Engineering

SAMEH NAZMI HELMI ALJAMAL

DEPARTMENT OF INDUSTRIAL AND MATERIALS SCIENCE

---

CHALMERS UNIVERSITY OF TECHNOLOGY

Gothenburg, Sweden 2019

[www.chalmers.se](http://www.chalmers.se)



REPORT NO. 2019/1030

# Process Optimization of Additive Manufacturing of Tool Steels

**SAMEH NAZMI HELMI ALJAMAL**



**CHALMERS**  
UNIVERSITY OF TECHNOLOGY

Department of Industrial and Materials Science

CHALMERS UNIVERSITY OF TECHNOLOGY

Göteborg, Sweden 2019

Process Optimization of Additive Manufacturing of Tool Steels

SAMEH NAZMI HELMI ALJAMAL

© SAMEH NAZMI HELMI ALJAMAL, 2019.

Examiner and Supervisor: Yu Cao, Chalmers University of Technology.

Supervisor: Christophe Lyphout, RISE IVF.

Technical report no 2019/1030

Department of Industrial and Materials Science

Chalmers University of Technology

SE-412 96 Göteborg Sweden

Telephone + 46 (0)31-772 1000

Cover: Lack of fusions presented in the microstructure, produced by RISE IVF.

Printed by Chalmers Reproservice

Göteborg, Sweden 2019

Process Optimization of Additive Manufacturing of Tool Steels

SAMEH NAZMI HELMI ALJAMAL

Department of Industrial and Materials Science

Chalmers University of Technology

## **SUMMARY**

Additive manufacturing is one of the growing fields in manufacturing industry. Selective laser melting is one of the techniques based on powder bed fusion and used normally for metallic materials. H13 tool steel is categorized as difficult – to – build materials, because the alloy carbides contained due to high amount of carbon make it difficult to melt and fuse. Another challenge is that the cooling rates in selective laser melting can reach as high as  $10^4$ - $10^6$  K/s, which affects the final properties of the printed part. Furthermore, the process parameters of selective laser melting affect the properties of the material.

This work studies the printing behavior of H13 tool steel with different process parameters for selective laser melting. The work aims to obtain the optimum process parameters. For this purpose, 71 samples are prepared and inspected in terms of porosity, microstructure, hardness and density by means of scanning electron microscopy, energy dispersive spectrometry, light optical microscopy and density measurements.

It is found that based on layer thickness, laser power, scanning speed and hatch distance can be selected. In conclusion, to achieve good printing results with 45  $\mu\text{m}$  and 60  $\mu\text{m}$  layer thickness, scanning speed and hatch distance should be low with high laser power. For 30  $\mu\text{m}$  layer thickness, laser power and scanning speed should be high and hatch distance should be low.

Keywords: Additive Manufacturing, Selective Laser Melting, H13 Tool Steel and Process Optimization.

## **Acknowledgement**

I would like to thank all the people who helped me during this journey especially my examiner and supervisor Prof. Yu Cao for providing all the help to accomplish this work to the best shape. I would like also to thank my supervisor at RISE IVF Dr. Christophe Lyphout for providing all the help that I need to accomplish the experimental work at RISE IVF. Also, I would like to thank all the people in additive manufacturing group at RISE IVF and the department of Industrial and Materials Science at Chalmers University of Technology for helping me during my thesis work.

Special thanks to my family who supported me and encouraged me to take this leap in my life, especially my lovely mother and my father who supported me strongly from my day of birth until now.

# Table of Contents

SUMMARY .....	i
Acknowledgement .....	ii
Table of Contents .....	iii
List of Figures .....	v
List of Tables .....	vi
CHAPTER 1 .....	1
Introduction.....	1
1.1    Review of Additive Manufacturing .....	1
1.2    Classification of Additive Manufacturing.....	3
1.3    Powder Bed Fusion .....	3
1.3.1    Fusion Mechanisms.....	4
1.3.2    Materials .....	4
1.3.3    Benefits and Drawbacks.....	5
1.3.4    Selective Laser Melting (SLM).....	6
1.4    Tool Steels .....	8
1.4.1    Important Alloying Elements in Tool Steels.....	8
1.4.2    Fabrication of Tool Steels .....	9
1.4.3    Tool Steel Selection .....	10
1.4.4    Grades and Classification of Tool Steels .....	10
1.4.5    Heat Treatment of Tool Steels .....	11
1.4.6    Tool steels in Powder Metallurgy .....	12
1.4.7    H13 Tool Steel .....	13
1.5    Objectives .....	13
CHAPTER 2 .....	14
Experimental Work.....	14
2.1    Sample Printing.....	14
2.2    Sample Preparation .....	15
2.3    Techniques for Microstructure Study .....	15
2.3.1    Scanning Electron Microscopy (SEM) .....	16
2.3.2    Energy Dispersive Spectroscopy (EDS) .....	16
2.4    Hardness and Density Measurements .....	17
2.5    Porosity Measurements .....	19

CHAPTER 3 .....	20
Results and Discussion .....	20
3.1    Microstructure (Optical Microscopy) .....	20
3.1.1    Effect of Layer Thickness .....	21
3.1.2    Effect of Hatch Distance .....	27
3.1.3    Effect of Laser Power and Scanning Speed .....	27
3.1.4    Combined Effect of Laser Power, Scanning Speed, Hatch Distance and Layer Thickness	30
3.2    Porosity Measurements .....	31
3.2.1    Effect of Printing Parameters on the Number of Defects .....	31
3.2.2    Pores and Lack of Fusion .....	34
3.2.3    Average Size of Pores .....	36
3.3    Hardness.....	37
3.3.1    Effect of Layer Thickness on Hardness .....	38
3.3.2    Effect of Laser Power and Scanning Speed on Hardness .....	38
3.3.3    Effect of Hatch Distance on Hardness .....	39
3.3.4    Average Hardness Along Building Direction .....	40
3.4    Density .....	40
3.5    Preliminary information of Chemical Composition.....	42
CHAPTER 4 .....	43
Conclusion and Remarks .....	43
CHAPTER 5 .....	44
Future Work.....	44
References.....	45
Appendix – A.....	47
Appendix – B.....	50

# List of Figures

<i>Fig 1-1: Process steps for additive manufacturing technology (Courtesy to research institute of Sweden (RISE IVF)).</i>	2
<i>Fig 1-2: Temperature gradient causing residual stresses (Top) and the resulting cracks in the structure (Bottom) (Courtesy to Yap et al).</i>	7
<i>Fig 1-3: Comparison between different tool steel grades (Courtesy to ASM International).</i>	10
<i>Fig 1-4: Tempering effect on secondary hardening for some tool steels (Courtesy to ASM International).</i>	12
<i>Fig 2-1: The printed cubes (71 cubes with 30 <math>\mu\text{m}</math>, 45 <math>\mu\text{m}</math> and 60 <math>\mu\text{m}</math> layer thicknesses).</i>	14
<i>Fig 2-2: Interaction volume.</i>	16
<i>Fig 2-3: The main mechanism of EDS.</i>	16
<i>Fig 2-4: Characteristic x-ray detection principle.</i>	16
<i>Fig 2-5: Archimedes principle for finding the density of the cubes.</i>	17
<i>Fig 2-6: Indentation map on sample's cross-section.</i>	18
<i>Fig 2-7: Average hardness line in the x-direction.</i>	18
<i>Fig 2-8: Average hardness line in the z-direction.</i>	19
<i>Fig 3-1: Microstructure of sample R3 at 5x magnification.</i>	20
<i>Fig 3-2: Samples' microstructure at 5x magnification: (a) sample R1 (30 <math>\mu\text{m}</math> layer thickness) and (b) sample R5 (60 <math>\mu\text{m}</math> layer thickness).</i>	21
<i>Fig 3-3: SEM images of the samples in Table 3-1.</i>	24
<i>Fig 3-4: Melting pool in sample R2 (30 <math>\mu\text{m}</math>).</i>	25
<i>Fig 3-5: Melting pool in sample R9 (45 <math>\mu\text{m}</math>).</i>	26
<i>Fig 3-6: Melting pool in sample R5 (60 <math>\mu\text{m}</math>).</i>	26
<i>Fig 3-7: Difference in defects between different hatch distances: (a) sample No.25 (0.14 mm), (b) sample No.29 (0.10 mm).</i>	27
<i>Fig 3-8: Defects in sample R5 with laser power of 150 W and scanning speed of 650 mm/s.</i>	28
<i>Fig 3-9: Defects in sample R6 with laser power of 250 W and scanning speed of 650 mm/s.</i>	29
<i>Fig 3-10: Defects in sample R7 with laser power of 150 W and scanning speed of 900 mm/s.</i>	29
<i>Fig 3-11: Defects in sample R8 with laser power of 250 W and scanning speed of 900 mm/s.</i>	30
<i>Fig 3-12: Lack of fusions in samples (a) No. 07, (b) No. 27 and (c) No. 47. (30 <math>\mu\text{m}</math>, 60 <math>\mu\text{m}</math> and 45 <math>\mu\text{m}</math> respectively).</i>	36
<i>Fig 3-13: The shape of pores in the microstructure. (a) sample R2 (30 <math>\mu\text{m}</math>) and (b) sample R3 (30 <math>\mu\text{m}</math>).</i>	37
<i>Fig 3-14: Inaccurate hardness measurements for sample R7 with 60 <math>\mu\text{m}</math> layer thickness.</i>	38
<i>Fig 3-15: Location of EDX analysis on sample R2.</i>	42
<i>Fig B-1: None melted powder and lack of fusion for sample R5 (60 <math>\mu\text{m}</math> layer thickness).</i>	50
<i>Fig B-2: Lack of fusion for sample R7 (60 <math>\mu\text{m}</math> layer thickness).</i>	50
<i>Fig B-3: Lack of fusion for sample R9 (45 <math>\mu\text{m}</math> layer thickness).</i>	51
<i>Fig B-4: defects free microstructure for sample R1 (30 <math>\mu\text{m}</math> layer thickness).</i>	51

# List of Tables

<i>Table 1-1: AISI classification of tool steels.</i>	11
<i>Table 2-1: Chemical composition of used H13 tool steel in this research work.</i>	14
<i>Table 2-2: Used values for SLM parameters.</i>	15
<i>Table 2-3: Naming system of the samples.</i>	15
<i>Table 3-1: Representation of the laser power and scanning speed for R samples.</i>	22
<i>Table 3-2: Comparison of the total amount of defects between different layer thicknesses.</i>	32
<i>Table 3-3: Comparison of the total amount of defects between different laser power and scanning speed (first group).</i>	32
<i>Table 3-4: Comparison of the total amount of defects between different laser power and scanning speed (second group).</i>	32
<i>Table 3-5: Comparison of the total amount of defects between different laser power and scanning speed (third group).</i>	33
<i>Table 3-6: Comparison of the total amount of defects between different laser power and scanning speed (fourth group).</i>	33
<i>Table 3-7: Comparison of the total amount of defects between different hatch distances (first group). Hatch distance: 0.10 mm</i>	33
<i>Table 3-8: Comparison of the total amount of defects between different hatch distances (second group). Hatch distance: 0.14 mm</i>	34
<i>Table 3-9: Number of pores for samples with different layer thickness, hatch distance, scanning speed and laser power.</i>	35
<i>Table 3-10: Number of lack of fusions for samples with different layer thickness, hatch distance, scanning speed and laser power.</i>	35
<i>Table 3-11: Average hardness for samples with different layer thickness.</i>	38
<i>Table 3-12: Average hardness for samples with different laser power and scanning speed (first group).</i>	38
<i>Table 3-13: Average hardness values for samples with different laser power and scanning speed (second group).</i>	38
<i>Table 3-14: Average hardness values for samples with different laser power and scanning speed (third group).</i>	39
<i>Table 3-15: Average hardness values for samples with different laser power and scanning speed (fourth group).</i>	39
<i>Table 3-16: Average hardness for samples with different hatch distance (first group).</i>	39
<i>Table 3-17: Average hardness for samples with different hatch distance (second group).</i>	39
<i>Table 3-18: Average hardness in z-axis (building direction).</i>	40
<i>Table 3-19: Density ratios of the printed samples to the raw powder material.</i>	41
<i>Table 3-20: Chemical composition at different locations in sample R2 (wt%).</i>	42
<i>Table A-1: Density ratios between the printed samples and the original density of the powder material.</i>	47
<i>Table A-2: Pores average size for all the samples.</i>	48
<i>Table A-3: Mean hardness values for all the samples.</i>	49

# CHAPTER 1

## Introduction

The modern manufacturing has become a highly technical and challenging field with engineering projects around the world. Current manufacturing methods such as machining, deep drawing, stamping, casting and others are developed all over the years. These developments concerned about increasing the production, supporting new geometries, implementing automation in the production lines and much more [1]. However, these manufacturing methods have limitations in many aspects such as producing complex geometries, as an example, it is not easy to manufacture cooling channels inside injection molding tools (dies and molds), or produce metallic foams for energy absorption parts such as bumper beams and crash boxes. For these reasons, it is important to explore new and robust manufacturing technology [2].

Current manufacturing is in general based on subtractive methods. This means tools are used to remove the material in order to create the desired shape or design. And mostly, it begins with round bars or blocks as raw materials. Furthermore, the commonly used cutting, drilling and milling tools are not flexible to form complex shapes or have the ability to form extremely fine structures. Although casting can be used to form complex shapes, it is limited by the molds which are manufactured by machining or by any other method [3].

For these reasons, it is important to develop new methods. Additive manufacturing (AM) is one of them. As defined by American Society for Testing and Materials (ASTM), AM is a process of joining materials to make objects from computer aided design (CAD) usually layer upon layer, as opposed to subtractive manufacturing methodologies [4].

### 1.1 Review of Additive Manufacturing

Additive manufacturing is one of the new manufacturing methods that are currently used. It is a revolution of rapid prototyping (RP). In industries, this term was used to describe the process for creating initial/rapid parts for demonstration before producing the final or commercialized parts. However, it has been realized that this term is not able to fully describe the recent development and the term additive manufacturing is used instead. Also, it is inaccurate to say that AM technology is only applicable for making models, since AM can be used in a conjunction with other technologies to form a process chain, which will shorten product manufacturing time significantly.

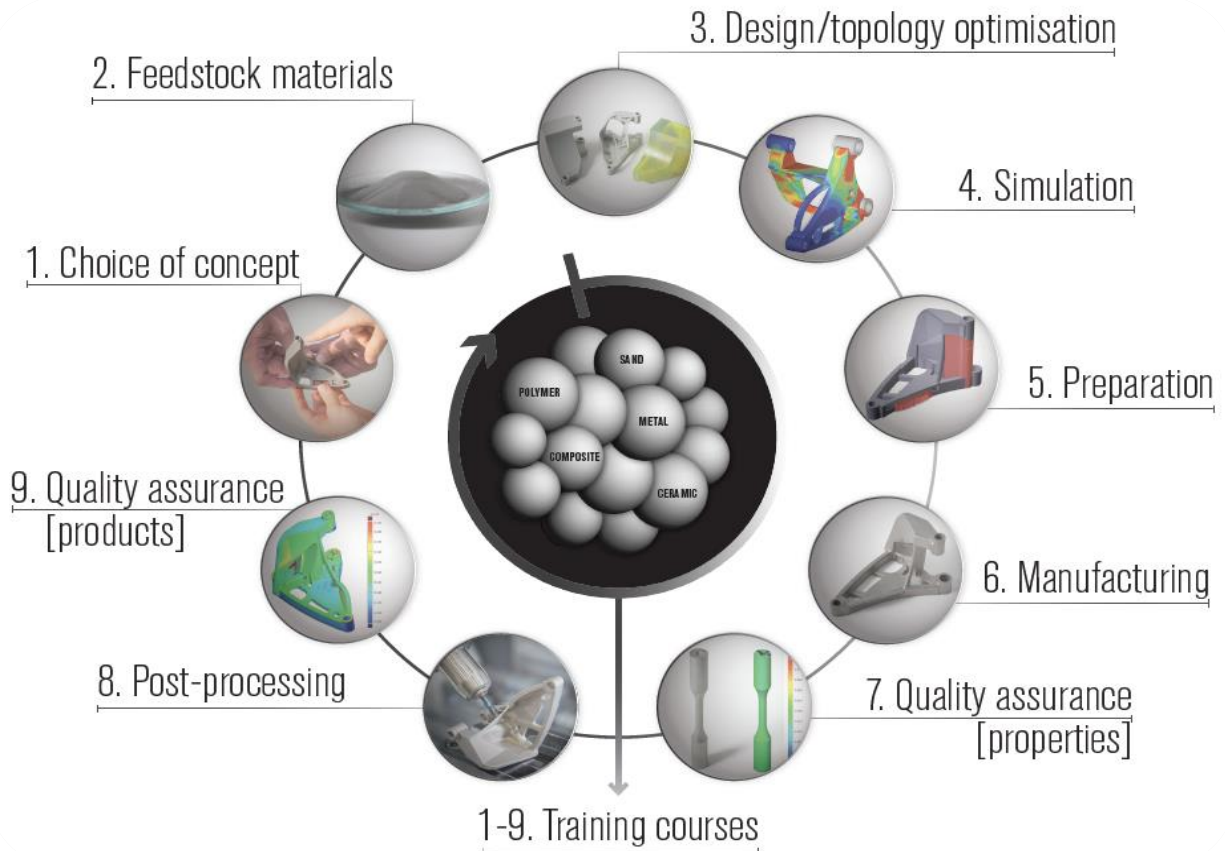


**Fig 1-1: Process steps for additive manufacturing technology (Courtesy to research institute of Sweden (RISE IVF)).**

Furthermore, some AM processes have been developed in order to produce a ready to use products. For these reasons the terminology changed from rapid prototyping to additive manufacturing. Compared to conventional manufacturing methods, one of the benefits in AM technology is the capability of fabricating complex three-dimensional (3D) shapes [5].

AM includes several steps in order to convert the model from CAD file to a functional product as shown in Fig 1-1 and explained as follows [5]:

- A CAD file for the part is prepared first.
- CAD file is converted to a standard tessellation language (STL) file which is a meshed model that is understandable by the machine and its software. The function of STL files is to correct:
  - The size.
  - The position.
  - The orientation of the product.
- Proper parameters for the printing will be selected based on the material used, the source of energy used, the thickness of the layer etc.
- Monitoring during the printing is necessary in order to make sure that the build process is going well.
- Depending on the method used and the material, the part will be removed either by machining or by hand.

- A necessary post processing such as machining or heat treatment will be performed.

Currently, additive manufacturing has attracted the interest of many industries such as aerospace, medicine, automotive, jewelry and other fields due to the benefits listed below [5]:

- AM allows to have a physical part converted directly from 3D CAD drawing of a component.
- AM allows part generation with great customization, without an additional cost, such as additional manufacturing cost when it comes to tooling.
- With AM it is possible to design for function rather than for manufacturing. For example, internal features such as complicated cooling channels for tools would be impossible using current manufacturing techniques.
- AM enable the production of lightweight structures by creating novel designs and using flexible manufacturing.
- AM has the ability to produce components to their final (net) shape or with minimal need of process steps.
- When it comes to manufacturing waste, AM techniques can reach zero waste regarding material utilization as the powder is re-used.
- None of AM techniques directly use toxic chemicals compared to other manufacturing processes, which is a direct benefit of AM.
- AM can combine several steps into a single manufacturing step which will decrease the overall manufacturing duration compared to traditional manufacturing methods.

This method can be a good alternative for conventional manufacturing methods, even though it is still under development and it has not reach high mass production ability as in other manufacturing processes.

## **1.2 Classification of Additive Manufacturing**

AM technology are categorized as per ASTM to seven different processes [5]:

1. Vat Photo-polymerization.
2. Powder Bed Fusion.
3. Material Extrusion.
4. Material Jetting.
5. Binder Jetting.
6. Direct Energy Deposition.
7. Sheet Lamination.

This work focuses on a powder bed fusion process → selective laser melting (SLM).

## **1.3 Powder Bed Fusion**

Powder Bed Fusion (PBF) is an additive manufacturing process using laser or electron beam as heat source which selectively melts certain regions of the powder bed. The main methods of PBF are selective laser melting and electron beam melting (EBM). Other methods are in one way or another based on the need in terms of machine productivity, the properties needed or the features that to be avoided. The working principle of SLM is that the powder is fused as thin layers using

leveling blade or roller which spreads the powder across the build area in a chamber filled with a certain protective gas. The gas used inside the building chamber depends on the powder used and the thermal power as well. For example, in metal selective laser melting, the gas used is noble Argon (Ar) while in polymer laser sintering the gas used is Nitrogen (N<sub>2</sub>) [5].

### 1.3.1 Fusion Mechanisms

PBF has four different fusion mechanisms; these mechanisms are listed as follows:

- **Solid – State Sintering:** The usage of the word “Sintering” might be a confusion. Sintering process means that the fusion occurs without melting. Powder particles are heated to a temperature between half of the absolute melting temperature and the melting temperature. Therefore, the powder is still in solid state. The driving force for solid – state sintering is to minimize the total free surface energy ( $E_s$ ) of the particles, which is directly proportional to the surface area and the surface energy per unit area as shown in the following formula:

$$E_s = \gamma_s \times S_A \quad (1)$$

Where,

$E_s$ : Total free surface energy of the particles

$S_A$ : Surface area

$\gamma_s$ : Surface energy per unit area

As the total surface area of the particles decreases, the surface energy decreases as well. This requires high sintering temperatures and long sintering times which slows the process [5].

- **Chemically Induced Sintering:** It is a type of sintering in which a thermally activated reaction occurs between two types of powders or between a powder and the surrounding gas. This will end up by forming a final product that differ from the original powder. This type of sintering is mostly used for ceramic powder [5].
- **Liquid – Phase Sintering and Partial Melting:** In this mechanism, a portion of the powder will be melted while the other portion will remain solid. The molten material will act as glue which binds the solid powder together without direct melting or sintering for the particles [5].
- **Full Melting:** This mechanism is commonly associated with PBF processing for metal alloys and semi – crystalline polymers. The subjected heat energy from laser beam or electron beam will melt the material to a depth exceeding layer thickness. And several scans of laser or electron beam will re-melt previously solidified layer in order to bond with the newly added layer [5].

### 1.3.2 Materials

The materials can be manufactured by PBF can be categorized as follows:

- **Polymers:** There are two different types of polymers which are thermoplastics and thermo-sets. Thermoplastics are the mostly used in PBF systems. The reason behind that is that thermo-sets cannot melt as thermoplastics do; instead, they degrade as the

temperature rises. Amorphous thermoplastics have a wide range of melting points. However, it is important to have a defined melting point which can be achieved by increasing the level of crystallinity of thermoplastics. Semi-crystalline polyamides can be used. However, crystalline polymers produced by full melting which increases the density tend to shrink more compared to amorphous polymers, leading to highly porous shape [5].

- Metals: many types of metals including stainless and tool steels, titanium and its alloys, nickel – based alloys, some aluminum alloys and cobalt – chromium alloys are used in PBF, especially the ones used in welding because of their ability of diffusion when they are exposed to a heat source. In addition, gold and silver are used as well to produce jewelry [5].
- Ceramics: briefly, these materials can be described as compounds of metallic oxides, carbides and nitrides and their combinations [5].

### **1.3.3 Benefits and Drawbacks**

#### **Benefits (polymers and metals) [5]:**

- The ability of using a wide range of metals and polymers.
- In the case of polymers, complex geometries and features can be manufactured without support structures.
- For metals, excellent mechanical properties can be achieved compared to traditional forming processes.

#### **Drawbacks (polymers and metals) [5]:**

- Polymers produced by PBF has poor accuracy and surface finish when it is compared with liquid-based processes.
- Unlike polymers, support structures are needed in metals when generating complex geometries.
- Machining process is needed for metallic parts produced by PBF because of the poor surface finish.
- More time and cost will be needed for metals produced by PBF because of the necessary support structure.
- It is time consuming in the design stage for metals because the processes depend on the orientation of the part and the location of support structures.

Many industrial systems use powder bed fusion process including selective laser melting, EBM, selective laser sintering, high speed sintering and selective mask sintering. This work focusses on selective laser melting.

### 1.3.4 Selective Laser Melting (SLM)

Selective laser melting is an additive manufacturing process based on powder bed fusion method. It is similar to selective laser sintering (SLS) except that in SLM the material is fully melted. As in all additive manufacturing processes, SLM process starts by preparing CAD files and ending with printing the full part as illustrated previously in Fig 1-1. After printing, the loose powder is removed from building chamber followed by electrical discharge machining (EDM) to remove the part from the build plate. Normally, the building chamber is filled with an inert gas such as nitrogen or argon to protect the heated material from oxidation in the process [6].

During SLM process, the powder material exposed to laser beam is heated and melted. Rapid solidification of the printed part means that the cooling rates in SLM process are high [7].

There are several significant physical phenomena associated with the printing process. For SLM, the phenomena that should be taken into consideration include powder material absorptivity of laser irradiation, balling and thermal fluctuation which is experienced by the material. Regarding material interaction with laser beam, four important printing parameters considered in this work are laser power, scanning speed, hatch distance and layer thickness [8]. These parameters affect the energy density per unit volume which is responsible for the heating and melting of the powder. Normally, insufficient energy is caused by the combination of low laser power, high scanning speed and large layer thickness [9], leading to balling due to the lack of wetting of the melted powder with the preceding layer. However, high laser power and low scanning speeds will result in extensive evaporation of the material and keyhole effect in the microstructure. Furthermore, extensive vaporization will cause the condensation of volatilized materials on the glass cover of the laser. In addition, improper hatching may result in porosity which will cause improper fusion between melt lines. In summary, proper printing parameters are important in order to obtain a near net full-density part. The mathematical expression of the energy density is shown in Equation (2) [9].

$$E = \frac{P}{v \cdot h \cdot t} \text{ [J/mm}^3\text{]} \quad (2)$$

Where,  $E$ : energy density,  $h$ : hatch distance,  $t$ : layer thickness,  $P$ : laser power and  $v$ : scanning speed (laser velocity).

Other parameters such as scanning pattern, preheating and controlling of the cooling rates may also influence the final mechanical properties and the microstructure of the printed part by changing the energy density and consequently the way of material fusion and the number of pores that may appear in the microstructure [9].

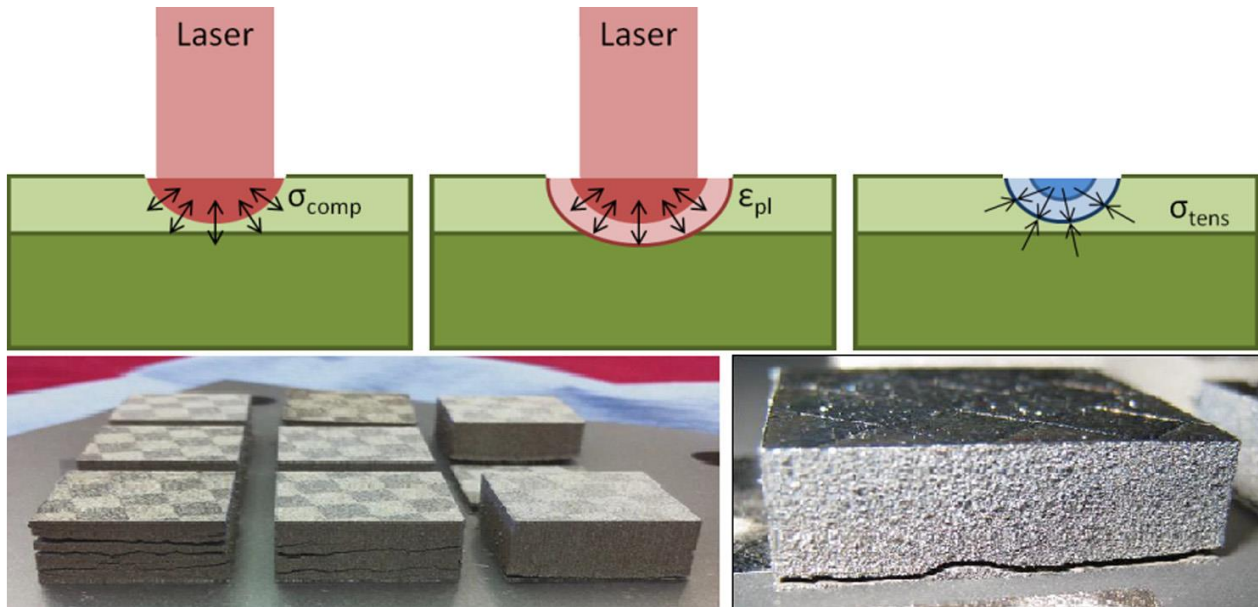


*Fig 1-2: Temperature gradient causing residual stresses (Top) and the resulting cracks in the structure (Bottom) (Courtesy to Yap et al).*

Another important effect is balling which occurs due to insufficient wetting with the preceding layer and surface tension, leading to the formation of spheroidal beads. Balling is not preferable because it prevents the formation of continuous melt lines, leading to a rough surface and a bad shape. In some of the worst cases, balling can form big beads that will extend above the powder bed and cause jamming for the re-coater [9]. Moreover, Fig 1-2 shows that when the material is subjected to laser beam, it will have compressive residual stresses and plastic deformation. And during cooling, the residual stresses will be converted to tensile stresses. These residual stresses are a result of the variable extent of thermal fluctuation. This in turn cause crack initiation in the printed part as shown in Fig 1-2 [9].

#### **1.3.4.1 Materials for SLM Process**

There is a wide variety of the materials that can be printed by SLM, mostly are the metals and their alloys. Composites and ceramics can also be produced by SLM. Below is a list of the most used materials with SLM [9]:

- Steels and iron-based Alloys: 316L Stainless Steel, M2 High Speed Steel (Tool Steel), H13 Tool Steel and 314S Stainless Steel.
- Titanium and its Alloys: pure titanium, Ti-6Al-4V alloy (Ti64), Ti-6Al-7Nb, Ti-24Nb-4Zr-8Sn, Ti-13Zr-Nb, and Ti-13Nb-13Zr.
- Inconel and nickel-based alloys: Inconel 625, Inconel 718, Chromel, Hastelloy X, Nimonic 263, IN738LC, and MAR-M 247.
- Other metals: aluminum alloy (AlSi10Mg), pure aluminum, Al6061, AlSi12, AlMg, gold, silver, tantalum, and cobalt-chromium alloy.
- Ceramics:  $\text{Li}_2\text{O-Al}_2\text{O}_3\text{-SiO}_2$  (LAS) glass, alumina ( $\text{Al}_2\text{O}_3$ ), silica ( $\text{SiO}_2$ ), yttria-stabilized zirconia (YSZ), tri-calcium-phosphate (TCP), alumina-zirconia mixtures, dental porcelain, alumina-silica mixture, silicon carbide, and silicon monoxide.
- Composites: nickel superalloy Mar-M-247, cobalt braze alloy Amdry 788.

#### ***1.3.4.2 Influence of SLM Process on the Microstructure and the Mechanical Properties***

The microstructure is influenced by printing parameters, the chemical composition and thermal history. However, these parameters are correlated to each other. Mostly, process parameters are determined by the chemical composition to a large extent. On the other hand, the process parameters will affect the thermal history of the material. Repeated heating and fast cooling lead to non-equilibrium phases. Another effect of high cooling rates is the fine microstructure [10].

The density of the printed part in most cases varies between 97%-99.5%, which means that SLM can produce parts with almost full density. In a SLM process, the surrounding powder may be partially melted and stick on the outer surface of the part, leading to less good surface finish. This is one of the main drawbacks of SLM [10].

Compared to conventionally manufactured material, SLM is characterized by large temperature gradient and high cooling rates. This causes non-equilibrium at the solid/liquid interface, which leads to rapid solidification as melting pool undergoes transformation from liquid to solid. As a result, wide range of effects might occur such as the presence of defects, high hardness and strength, low toughness and non-equilibrium phases. Conventionally manufactured materials can have non-equilibrium phases. However, the tendency of these phases to present in SLM manufactured materials will be more than conventionally manufactured materials because of high temperature gradient and high cooling rates in SLM [10].

#### ***1.3.4.3 SLM and Porosity***

Based on the printing parameters, the energy density will affect the appearance of porosities and lack of fusion in the material. Mostly, lack of fusion is formed between the layers, specifically in x-y plane. This happens when the density of the energy is low. It is important to mention that pores resulted from lack of fusion are not regular in shape in most cases. Pores can also be formed due to the entrapped gas bubbles between the layers, and they mostly have circular cross-section or oval cross-section. When there is much turbulence in the melting pool, gas bubble will trap and cause a void. Furthermore, excessive shrinkage due to insufficient feeding of the material will cause the occurrence of pores as well. In general, voids from lack of fusion or entrapped bubbles are the initiation sites of cracks because of the residual stresses [11].

### **1.4 Tool Steels**

Tool steels are one type of steels that are used in producing tools for cutting, forming, shaping and machining. High hardness and durability are the main requirement.

#### **1.4.1 Important Alloying Elements in Tool Steels**

Tool steels are characterized by their high carbon content compared to other types of steels. The diversity in the properties comes from the different amounts and types of the alloying elements contained in the tool steel [12]. The most common and important alloying elements for tool steel are carbon, tungsten, chromium, vanadium and molybdenum. The benefits of alloying elements in tool steels are listed below.

- Carbon (C): It is the most important alloying element because it is connected to the strength and the hardness of the material by carbides formation, and in turn it will affect the wear resistance of the material. Also, carbon is an austenite stabilizer and it increases the

hardenability (capability of martensite formation) and consequently the strength of the material [13].

- Silicon (Si): The maximum allowed silicon is up to 1.00 wt%. When it is increased from 0.15 wt% to 0.45 wt%, the attainable tempered hardness will increase to its maximum and the toughness will decrease slightly [13].
- Manganese (Mn): It is not used in high concentrations because of its effect on increasing brittleness and the risk of cracking during quenching [13].
- Chromium (Cr): It is added usually in a concentration of ~ 4.00 wt% for different grades of tool steels since it has an effect on the hardenability of the material. Chromium promotes ferritic microstructure and provides corrosion resistance [13].
- Tungsten (W): The contribution is to form complex carbides together with iron and carbon in order to increase the hardness and wear resistance. Also, tungsten affects secondary hardening and improves the red hardness of the material [13].
- Molybdenum (Mo): It forms  $M_6C$  carbides with iron and carbon as tungsten does. Notice it only has half of the atomic weight compared to W. Molybdenum enhances weldability, corrosion resistance of the material and hinders grain growth. During heat treatment, molybdenum has the ability to reduce the decarburization rate [13].
- Vanadium (V): It is the element responsible for forming extremely hard carbides which are more stable than  $M_3C$ ,  $M_{23}C$  and  $M_6C$  carbides. When balancing the vanadium with the carbon content, the hardness will increase which in turn increases the wear resistance. Relatively large amounts of vanadium will not affect the toughness significantly. In addition, vanadium has an effect on secondary hardening due to the precipitation of MC carbides [13].

#### **1.4.2 Fabrication of Tool Steels**

There are many ways to fabricate tool steels [14]:

- Wrought products: They are the major proportion of tool steel products. In this case, precision and control are important for high quality materials. Moreover, cleanliness should be ensured through special refining and secondary re-melting processes. Forging and rolling should be controlled carefully followed by inspection routines to ensure quality [14].
- Precision casting: Uniform properties in all directions are required. The expected directionality in this case makes the dimensional control in all directions important, especially when compared to wrought products. [14].
- Powder metallurgy: Tool steels produced in this way are expected to have a fine microstructure with uniform distribution of carbides and other inclusions. Rapid solidification can be used to avoid the formation of coarse and non-uniform microstructure as in the case of ingot casting. In terms of design, there is a huge freedom in the case of powder metallurgy route [14].

### 1.4.3 Tool Steel Selection

Based on the application, several properties should be considered when selecting tool steels. Some important ones are listed below and shown in Fig 1-3 [14]:

- Hardness.
- Wear Resistance.
- Toughness.
- Red-hardness.

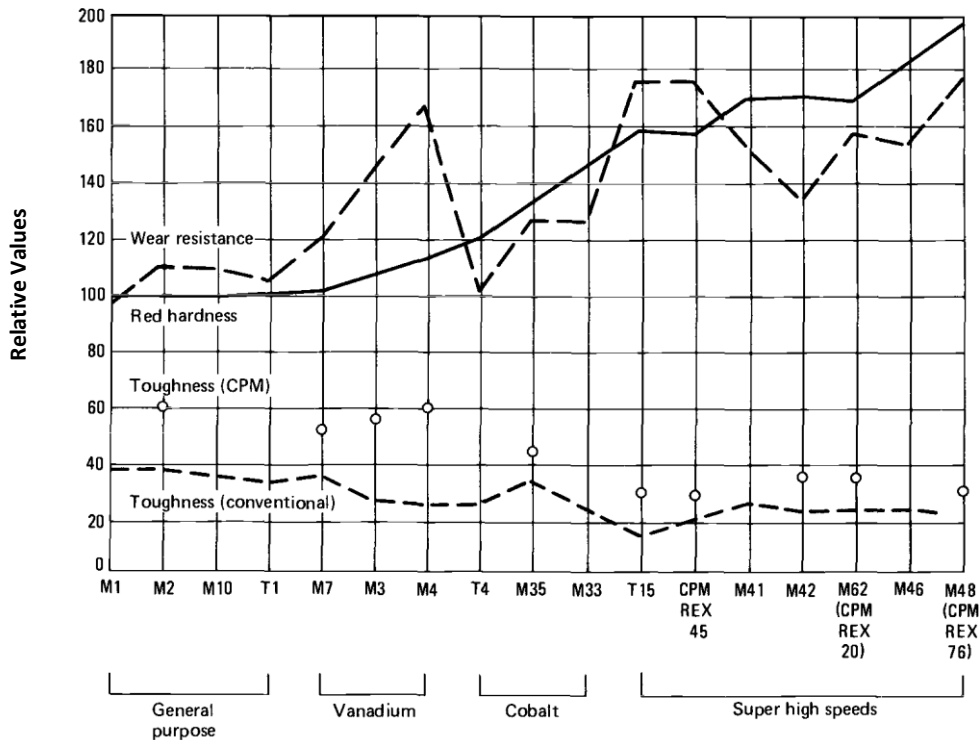


Fig 1-3: Comparison between different tool steel grades (Courtesy to ASM International).

### 1.4.4 Grades and Classification of Tool Steels

In general, tool steels are classified based on chemical composition, quenching media and the type of the application. Table 1-1 presents the classification of tool steels based on AISI (American Iron and Steel Institute) standard [14].

Table 1-1: AISI classification of tool steels.

Group	Symbol	AISI Type of Tool Steel
Water Hardening	W	-
Shock Resisting	S	-
Cold Work	O	Oil Hardening Cold Work
	A	Air Hardening, Medium Alloy
	D	High Carbon, High Chromium
Hot Work	H	Hot Work Tool Steel
High Speed	T	Tungsten High Speed
	M	Molybdenum High Speed
Mold	P	Mold Steels
Special Purpose	L	Low Alloy
	F	Carbon Tungsten

### 1.4.5 Heat Treatment of Tool Steels

During primary casting, a sequence of complex solidification is associated with tool steel, including the formation of delta ferrite and primary dendrites. Due to multicomponent alloying system, segregation of alloying elements takes place. In this case, a small ingot size is preferred, and the following hot working will decrease the size of the section [14].

After casting and hot working, annealing (spheroidizing) is performed in order to have a microstructure containing spheroidized carbides distributed homogeneously in the ferritic matrix. This form of the carbides is preferable for the subsequent processes such as hardening and machining. Furthermore, annealing is used to eliminate the hard phases that might present after hot working. Also, annealing promotes grain refinement and eliminates directionality from the microstructure. The annealing temperature is very critical, because it determines the distribution of alloying elements between the austenite matrix and the carbides which in turn determine the hardenability of the austenitic matrix. The choice of the annealing procedure can be predicted by the chemistry, the distribution and the size of the carbides [14].

Hardening is performed in order to form martensite and increase the hardness of tool steel by quenching in water or oil or cool by still air. The followed stress relief is to reduce residual stresses and crack initiation. Water hardened tool steels (W series from Table 1-1) have a hardening depth of around three millimeters with 780 °C, and it will increase to six millimeters in depth with 870 °C. The hardness values of W series tool steel can be more than 66 HRC (Rockwell hardness type C). Oil hardened tool steel (O series from Table 1-1) has hardening temperature ranging between 800 °C and 840 °C and its hardness will reach 66 HRC. Air hardened tool steel (A series from Table 1-1) has the least hardness compared to previous two categories, because the carbides will precipitate at the grain boundaries which leads to poor tool life. For air hardening, multiple tempering may be needed in order to transform the sluggish austenite and to increase the hardness while maintaining a good toughness [15].

In general, cooling after tempering is performed in air. Tempering temperature varies based on the type of steel and the designed application [16]. Tempering is used to increase toughness of the

tool steels after martensite is formed. However, in tool steel containing Cr, V, Mo etc., the story might be different. Curves 3 and 4 in Fig 1-4 represent the tempering response for steel grades such as A and M. At relatively high tempering temperatures, alloy carbides precipitate, leading to the increase of the hardness of the material, i.e., secondary hardening. In this case, toughness might be decreases. The grades of the steels for curves 1 and 2 in Fig 1-4 are W and O grades and S grade respectively. Secondary hardening is not observed due to the absence of alloying carbides, which leads to lower hardness compared to those from curves 3 and 4. [14].

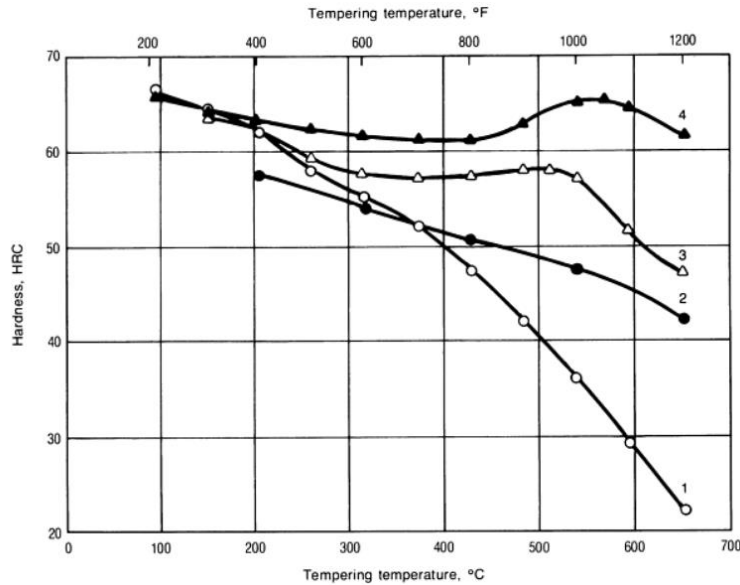


Fig 1-4: Tempering effect on secondary hardening for some tool steels (Courtesy to ASM International).

### 1.4.6 Tool steels in Powder Metallurgy

High alloy tool steels (HATS) consist of large amounts of alloying elements which forms hard phases in the microstructure during solidification. In powder metallurgy (PM) of HATS the powder is produced from the solidification of melt droplets. In this case the segregation of the elements is limited by the size of the particles. Sulfur and manganese are added sometimes to molten material before atomization in order to form manganese sulfide which are soft and malleable and can deform easily along the direction of the deformation. In PM, the microstructure is homogenous and this makes it possible to have a vanadium content more than 3%. Vanadium is an important element because of its ability to form stable and strong carbides. In normal cases, vanadium concentration does not exceed 3% [17].

The production of PM tool steels can be done with various techniques such as [17]:

- Spray forming followed by hot forming.
- Hot isostatic pressing (HIP) of nitrogen-atomized powders with subsequent hot working.
- Metal injection molding (MIM) of fine nitrogen-atomized powders which are sintered in vacuum (preferable) and then HIP is performed to reach full density (if required).
- Die compaction of binder-treated nitrogen-atomized powders followed by sintering and soft annealing. This usually followed by HIP.
- Die compaction of irregular vacuum annealed water-atomized powder and then vacuum sintering to full density, perhaps with additional HIP to improve the mechanical properties.

It can be said that the microstructure of PM tool steel is directional especially when hot worked particles are coarse or the microstructure contains sulfides [18].

### **1.4.7 H13 Tool Steel**

H13 is a chromium-molybdenum containing hot work tool steel. It is used widely as [19]:

- Inserts, cores, and cavities for die casting dies.
- Die casting shot sleeves.
- Hot forging dies.
- Extrusion dies, and plastic mold cavities and components that require high toughness and excellent polish ability.

H13 tool steel is excellent for hot work applications where cyclic cooling and heating are involved, since it has a high resistance to thermal fatigue cracking and relatively good toughness. It also has a high stability during heat treatment besides the good toughness, which makes it applicable for cold working. However, in SLM, H13 tool steel is one of what so called “difficult to build” materials because of its high hardness and brittleness, which makes it easy to crack due to thermal stress during SLM process. The common alloying elements presented in H13 tool steel are carbon, molybdenum, manganese, silicon, chromium and vanadium [20].

## **1.5 Objectives**

Many researches have been working on 3D printing of tool steels. H13 is classified as one of the hard-to-print materials because of its high carbon content which affects the fusion of the steel. High cooling rates in the SLM process make it even more challengeable due to thermal fatigue cracking and the appearance of porosities and lack of fusion. Defects such as cracks may initiate around the pores and lack of fusion areas because of the residual stresses [21]. In order to increase the process efficiency for tool steels or other hard-to-print materials, it is important to understand the effect of printing parameters on the printing behavior of the metallic materials [22].

The aim of the thesis work is to evaluate the impact of several critical process parameters such as laser power, scan speed, hatching distance, laser focus and layer thickness on the microstructure, hardness and density of the printed components with H13 tool steel. The process parameters that results in optimum microstructure of the printed parts will be selected for manufacturing tensile specimens to study the mechanical properties in the future. Questions to be answered are:

- What are the key process variables (KPVs) and their correlations with the material properties (porosity and hardness)?
- Is it possible to reduce porosity and internal cracks in tool steels by altering the KPVs at room temperature?
- What is the desired process window and how to improve productivity by increasing the layer thickness while keeping optimal material properties?

# CHAPTER 2

## Experimental Work

### 2.1 Sample Printing

For this specific research, the nominal composition of the material studied in weight percent is shown in Table 2-1 (Höganäs data sheet).

*Table 2-1: Chemical composition of used H13 tool steel in this research work.*

Element	Weight Percent (wt%)
Carbon	0.32
Molybdenum	1.34
Chromium	5.21
Silicon	0.90
Manganese	0.40
Vanadium	0.93

In order to understand the printing behavior of H13 tool steel and the effect of different process parameters, 71 cubes in total with a dimension of 10 mm × 10 mm × 10 mm were printed by selective laser melting process using SLM-Solutions 280 machine as shown in Fig 2-1.

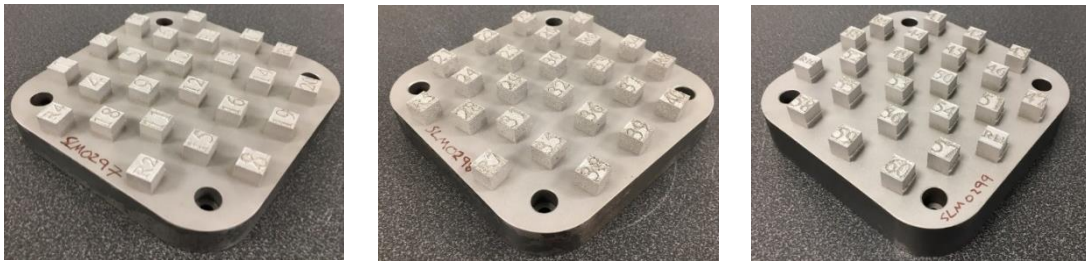


*Fig 2-1: The printed cubes (71 cubes with 30  $\mu$ m, 45  $\mu$ m and 60  $\mu$ m layer thicknesses).*

The build job was conducted in argon gas environment and the temperature of build plate was 200 °C. Selected process parameters were laser power, scanning speed, layer thickness and hatch distance and the used values are presented in Table 2-2.

*Table 2-2: Used values for SLM parameters.*

Process Parameter	Range of Values	Units
Layer Thickness	30, 45 and 60	µm
Laser Power	150, 200 and 250	W
Scanning Speed	650, 775 and 900	mm/s
Hatch Distance	0.10, 0.12 and 0.14	mm

For each layer thickness (30, 45 and 60 µm) there were 24 samples (except for 45 µm, it has 23 samples) which were divided into two groups as shown in Table 2-3. Hatch distance, scanning speed and laser power were varied, see Table 2-2. Samples R1 to R11 had the same hatch distance while it differed in samples No. 01 to No. 60.

*Table 2-3: Naming system of the samples.*

Layer Thickness (µm)	First Group of Samples	Second Group of Samples
30	R1 – R4	No. 01 – No. 20
60	R5 – R8	No. 21 – No. 40
45	R9 – R11	No. 41 – No. 60

## 2.2 Sample Preparation

After removing from the build plate, the samples were cut into two halves and then mounted using Polyfast resin for scanning electron microscopy (SEM) and light optical microscopy (LOM) observation because it is conductive. Subsequently, the sample was grinded with 220 grids and 320 grids sand papers. Afterwards, polishing was performed using diamond paste with particle sizes of 9 µm, 3 µm and OP-S. Finally, the samples were etched with an etchant called “Nital” (contains 5.0 ml HNO<sub>3</sub> and 95.0 ml methanol or ethanol).

## 2.3 Techniques for Microstructure Study

Microstructural investigation focuses on defects such as cracks, porosity and lack of fusion. “Leica DM4000 M” LOM is used to examine the melting pools, to compare the samples with different layer thicknesses and to determine the interesting areas for further inspection at high magnifications using SEM. Also, porosity measurements were performed by image processing in a circular area with a diameter of 9 mm. A series of images were taken in sequence. There was a contrast difference between the defects and the clean surface and dark areas represent pores and lack of fusion. The software will analyze the image and calculate the area fraction of defects. Moreover, SEM is used to examine the shape of the melting pools and the microstructure within and around the melting pool. In addition, the regions that have un-melted powders are investigated as well. Also, energy dispersive spectrometry (EDS) is used in order to know if there is any significant segregation of alloying elements.

### 2.3.1 Scanning Electron Microscopy (SEM)

It is a type of microscopy which uses an electron beam that scans the surface of the sample. As shown in Fig 2-2, the electron beam interacts with the sample, different signals are produced including Auger electrons, secondary electrons, backscattered electrons and characteristic X-Ray. These signals are detected by the detector. In the case of SEM, the most signals used are secondary electrons and backscattered electrons [23]. ZEISS GeminiSEM 450 is used in this work.

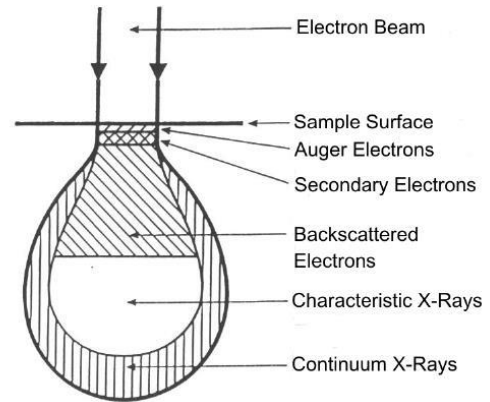


Fig 2-2: Interaction volume.

### 2.3.2 Energy Dispersive Spectroscopy (EDS)

Energy dispersive spectroscopy is a technique used for elemental analysis to find the chemical composition of the sample. Usually, EDS is mounted in high vacuum SEM (conventional instrument), TEM and FIB instruments.

The principle of characteristic x-ray generation (detected signal in EDS) is quite simple. When the electron beam with certain energy hits the surface of the sample an electron in the internal shells will be excited leaving an empty hole until it is filled by another electron from higher shell levels. This will create the characteristics x-ray because of the difference in energy levels between these two electrons [24]. Fig 2-3 displays the mechanism of characteristic x-ray generation.

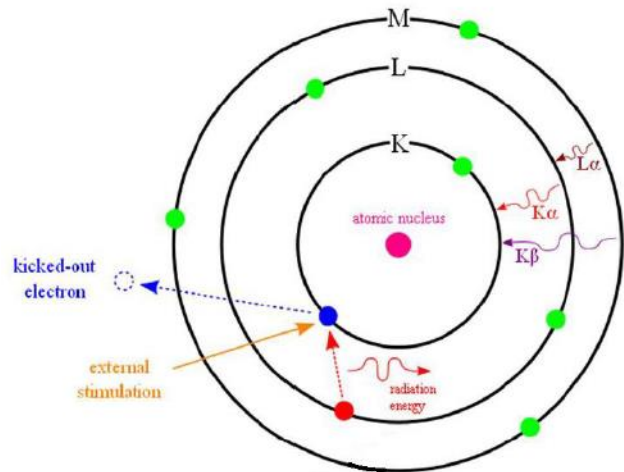


Fig 2-3: The main mechanism of EDS.

Characteristic x-ray is detected by a detector consisting of silicon crystals. Applying a high voltage on the entire silicon crystal will cause electrons and holes to move opposite to each other (electrons will move to one side of the crystal and holes will be to the opposite side). This will produce a charge signal that is processed by the pulse processor and converted to spectrums, as illustrated in Fig 2-4 [25].

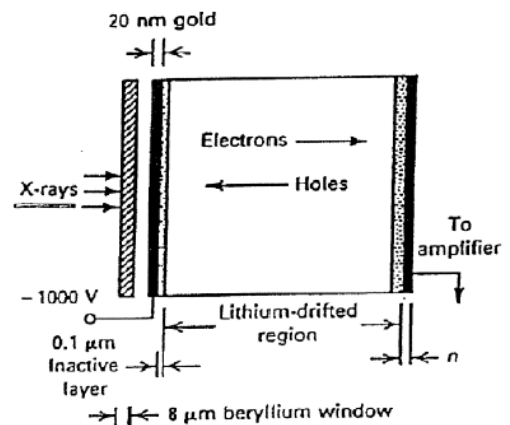


Fig 2-4: Characteristic x-ray detection principle.

## 2.4 Hardness and Density Measurements

Density measurements are performed by Höganäs AB using Archimedes method, as illustrated in Fig 2-5. The magnitude of the buoyant force acting on a body immersed into a fluid and the gravity force of the displaced fluid in the opposite direction is equal. By knowing the densities of the fluids ( $\rho_{water}$ ) and the weights of the body in air ( $m_{air}$ ) and in water ( $m_{water}$ ), the density of the solid ( $\rho_{obj}$ ) can be obtained [26]. The following equations (eq. 2-4) illustrate Archimedes principle.

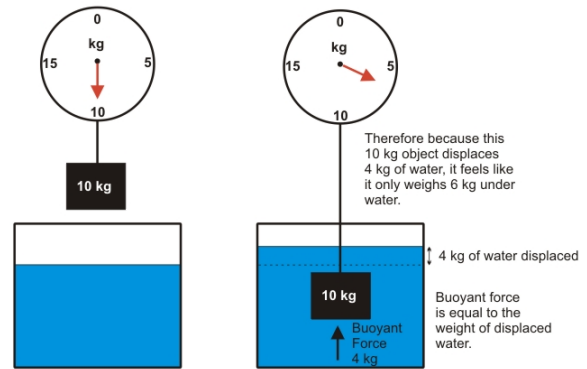


Fig 2-5: Archimedes principle for finding the density of the cubes.

$$V_{water\ displaced} = V_{obj} \quad (2)$$

$$V_{obj} = \frac{m_{water\ displaced}}{\rho_{water}} = \frac{m_{air} - m_{water}}{\rho_{water}} \quad (3)$$

$$\rho_{obj} = \frac{m_{air}}{(m_{air} - m_{water})} \times \rho_{water} \quad (4)$$

Where,

$V_{water\ displaced}$ : volume of the displaced water

$V_{obj}$ : volume of the object

$m_{water\ displaced}$ : mass of the displaced water

$m_{air}$ : mass of object in air

$m_{water}$ : mass of object in water

$\rho_{obj}$ : density of the object

$\rho_{water}$ : density of the water

Vickers Hardness (HV) measurements with 10 kg of load were conducted by defining an indentation map with 10 columns and 9 rows of indents as shown in Fig 2-6.

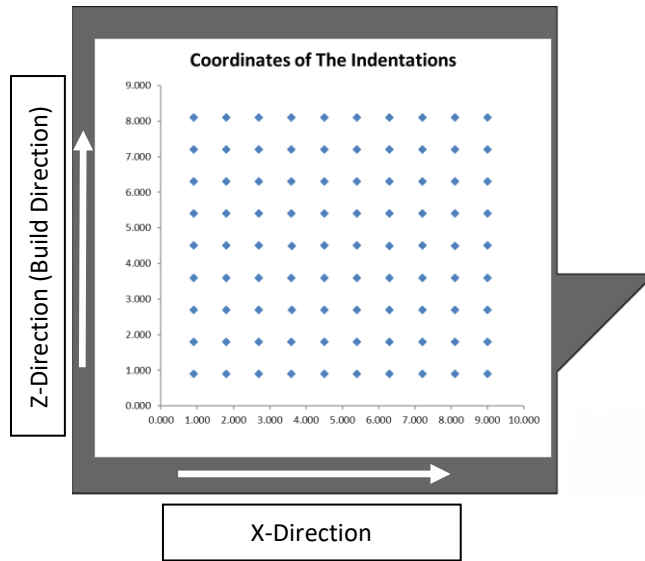


*Fig 2-6: Indentation map on sample's cross-section.*

Hardness measurements were performed on all the 71 samples. Average hardness in the x-direction and in the build direction (z-direction) were considered. The following procedure was followed to find the average line in the x-direction:

1. The average hardness of each column was calculated.
2. In total 10 average hardness values were obtained along X- direction (highlighted in **Horizontal Black Rectangle** in Fig 2-7).

The same procedure was performed in order to find the average line in the z-direction:

1. The average hardness of each row was calculated.
2. In total 9 average hardness values were obtained along building Z direction (highlighted in **Vertical Black Rectangle** in Fig 2-8).

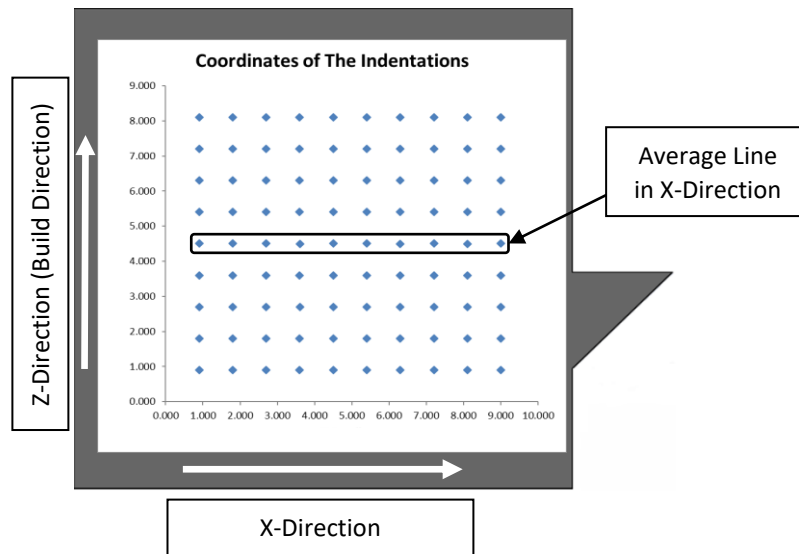


*Fig 2-7: Average hardness line in the x-direction.*

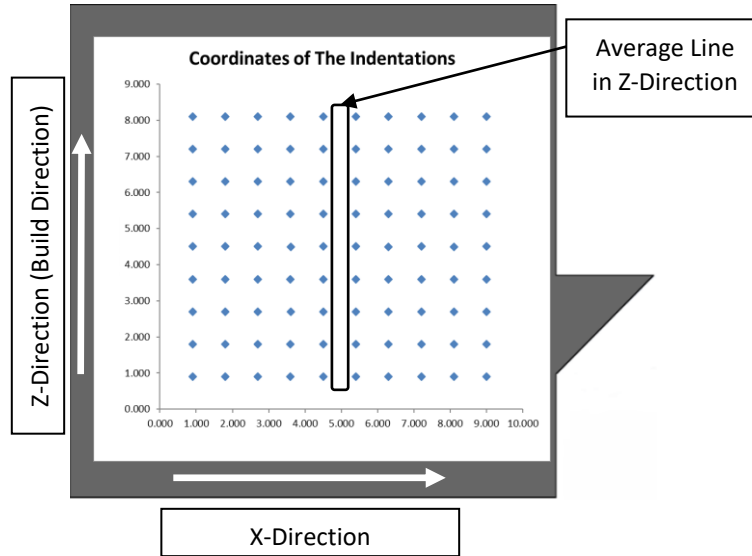


*Fig 2-8: Average hardness line in the z-direction.*

## 2.5 Porosity Measurements

Porosity measurements were conducted by scanning the sample surface using optical microscope. Mostly, the size of the pores is very small compared to size of lack of fusion. Recalling from the introduction, the creation of pores is initiated by the entrapment of gas bubbles inside the material. This occurs when there is so much turbulence in the melting pool. However, the creation of lack of fusions is depending on the lack of energy needed to melt the material.

In this section, the effect of the four printing parameters on the total amount of defects was considered separately.

To distinguish the pores from lack of fusion, it has been assumed that pores have circular or elliptical cross-section. The ratio of the length over the width is used to determine whether a defect is a pore or not. For a circular pore this ratio is equal to 1. A pore can also be elliptical in cross-section. In this study, a pore is defined as a defect having the ratio between 0.5 and 1.5. After the calculations for [0.5, 1.5] interval, [0.5, 1.2] and [0.5, 1.8] length over width ratio intervals were considered to check if there was a distinguished change in size distribution.

In the case of lack of fusion, it was assumed to have an elliptical cross-section with a ratio between 1.8 and 2.5. After the calculations for [1.8, 2.5] interval, [1.2, 2.5] and [1.5, 2.5] length over width ratio intervals were considered to check if there was a distinguished change in size distribution.

Image processing software (Leica) was used to find the average size of pores based on diameter of the defect.

# CHAPTER 3

## Results and Discussion

As an initial investigation, LOM, SEM and EDS are used to investigate the microstructure in general and to examine the effect of process parameters on the microstructure of the samples. Then, porosity and hardness are measured for all the samples and correlated with the microstructure.

### 3.1 Microstructure (Optical Microscopy)

Theoretically, the microstructure of the printed samples using SLM is predicted to be fine. Fig 3-1 shows the microstructure along the building direction. It has been observed that the melting pools overlap with each other. These pools are concaved upwards because the laser will re-melt the old layer while melting the new one, causing the molten material to fuse downwards as shown in the figure. According to Fig 3-1, the dark features in the microstructure are pores or lack of fusion because a pore or lack of fusion will create an empty area called “void”, this void will appear as a dark hole under the microscope because of the difference in contrast between the surface of the sample and the void.

It can also be seen from the figure that some melting pools are longer than others, as indicated by the solid black circles. The expected reason might be an excess of growth and a new melting pool overlapped on the older one due to discontinuous grain growth in which some grains grow quicker than others [27]. Lack of fusions are observed mostly between melting pools, i.e. in x-y plane between the layers as shown in the figure below (Fig 3-1). Also, the shape of lack of fusions is irregular, this differs from pores which are spherical or elliptical in shape.

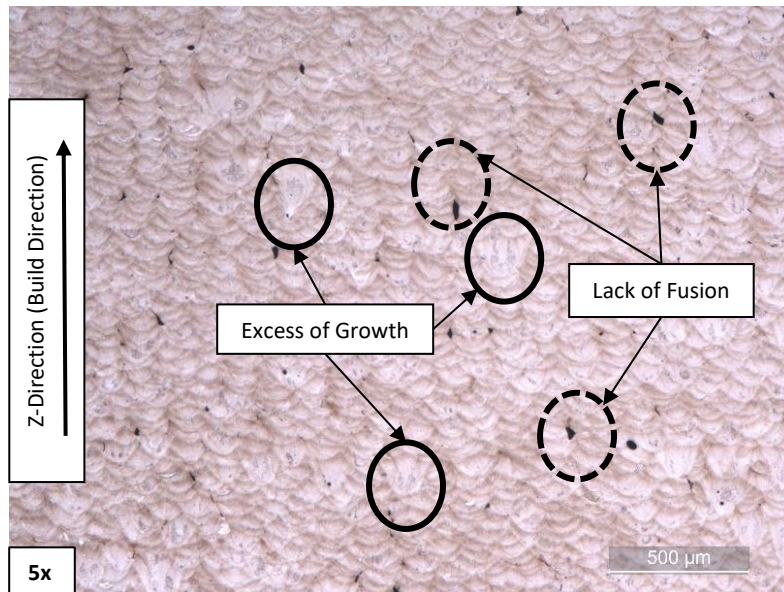


*Fig 3-1: Microstructure of sample R3 at 5x magnification.*

### 3.1.1 Effect of Layer Thickness

The sample in Table 3-1 are used to investigate the effect of layer thickness on the structure. Fig 3-2 shows the microstructure of two samples R1 and R5 at low magnification. They were prepared using same laser power, hatch distance and scanning speed but different layer thickness (30  $\mu\text{m}$  for R1 and 60  $\mu\text{m}$  for R5). The differences are huge. With high layer thickness as in R5, the microstructure suffered from large pores and lack of fusions as shown in Fig 3-2(b). However, as the thickness of the layer decreases, the fusion of the material increases as shown in Fig 3-2(a).

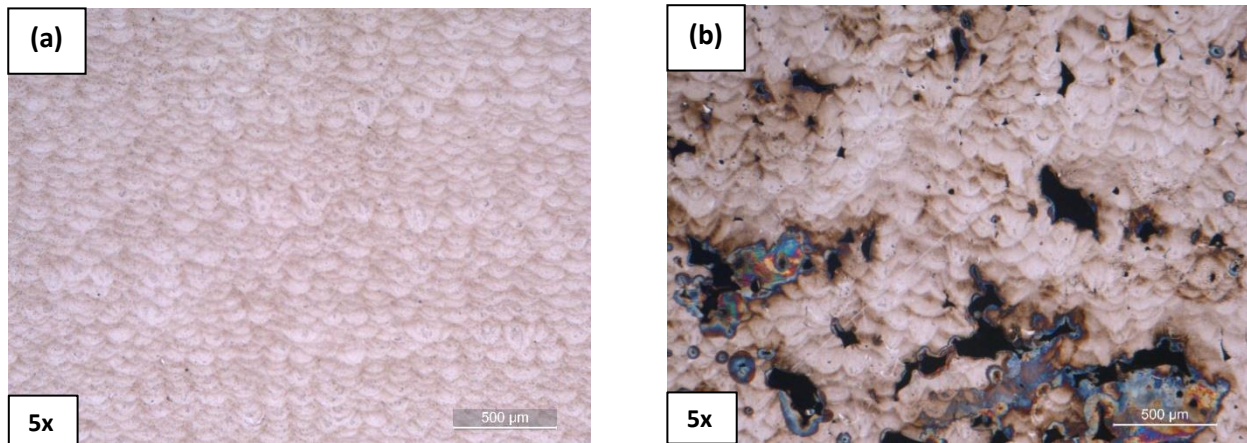


*Fig 3-2: Samples' microstructure at 5x magnification: (a) sample R1 (30  $\mu\text{m}$  layer thickness) and (b) sample R5 (60  $\mu\text{m}$  layer thickness).*

The observation is logical because sample R5 has larger layer thickness than R1. This means that R5 needs a higher amount of energy to melt the material compared to R1 sample. If the layer thickness is large, the resulted energy density is low based on eq. 2. In this case, although the upper portion of the laid material can be melted but the energy is not enough to melt completely the lower portion of the powder, leading to lack of fusion as shown in Fig 3-2(b).

Figures 3-3(a) to 3-3(k) are SEM images of the samples in Table 3-1, which further confirm the effect of changing layer thickness with different laser power and scanning speed. In general, with 30  $\mu\text{m}$  layer thickness, the number of defects is the least compared to 45  $\mu\text{m}$  and 60  $\mu\text{m}$  even with different laser power and scanning speed as shown in Figs 3-3(a), 3-3(b), 3-3(c) and 3-3(d). For 60  $\mu\text{m}$  samples, the number of defects is the highest and the size of the defects is the biggest, as shown in Figs 3-3(e), 3-3(f), 3-3(g) and 3-3(h). Lack of fusions were frequently observed, especially with R5 (low laser power and scanning speed) and R7 (low laser power and high scanning speed) samples. When it comes to 45  $\mu\text{m}$  layer thickness, the amount and the size of the defects are in between as in Figs 3-3(i), 3-3(j) and 3-3(k). Within the same layer thickness, the amount of defects changes based on laser power, hatch distance and scanning speed which will be discussed in details in the coming sections.

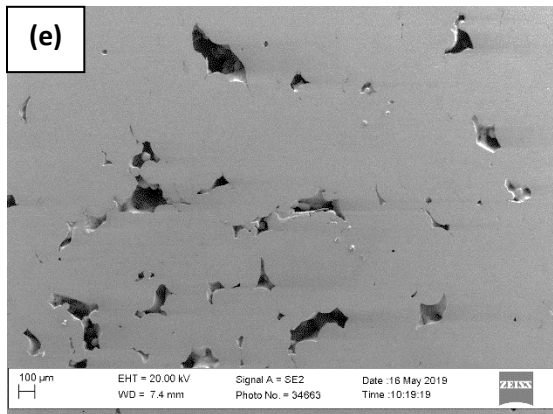
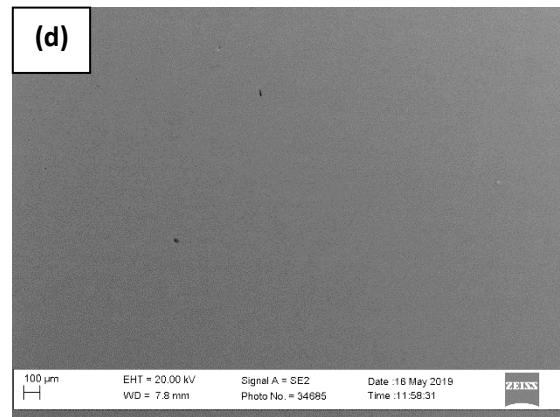
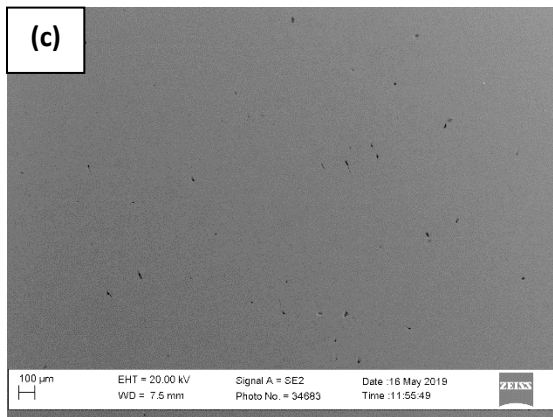
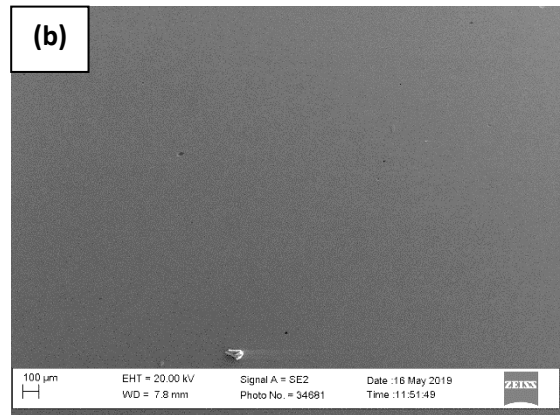
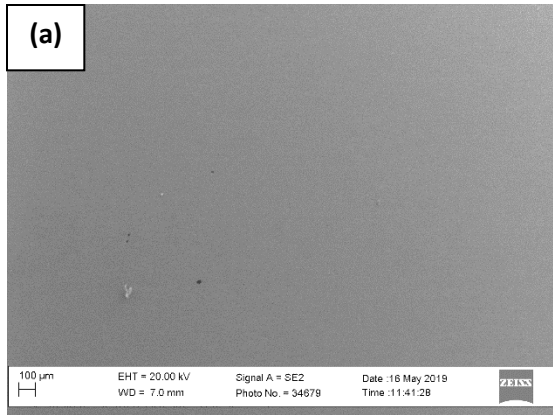
For 30  $\mu\text{m}$  layer thickness, samples R1 and R4 have the least number of defects compared to other samples with the same or different layer thickness. This is because the selected laser power and scanning speed are suitable for this layer thickness. For 60  $\mu\text{m}$ , R6 and R8 have relatively good microstructure but still it has more defect compared to R1 and R4 because large layer thickness needs more laser power to increase fusion. As to 45  $\mu\text{m}$ , R9, R10 and R11 have the same printing parameters. The amount of defects in their structure is not that much, even if they have less laser power but higher scanning speed than samples R6 and R8. All these observations indicate that layer thickness is a very important influencer.

*Table 3-1: Representation of the laser power and scanning speed for R samples.*

<b>Sample</b>	<b>Image No.</b>	<b>Laser Power</b>	<b>Scanning Speed</b>	<b>Layer Thickness</b>
<b>R1</b>	3-3(a)	C	Z	30
<b>R2</b>	3-3(b)	A	Z	30
<b>R3</b>	3-3(c)	C	X	30
<b>R4</b>	3-3(d)	A	X	30
<b>R5</b>	3-3(e)	C	Z	60
<b>R6</b>	3-3(f)	A	Z	60
<b>R7</b>	3-3(g)	C	X	60
<b>R8</b>	3-3(h)	A	X	60
<b>R9</b>	3-3(i)	B	Y	45
<b>R10</b>	3-3(j)	B	Y	45
<b>R11</b>	3-3(k)	B	Y	45

Where,  $A > B > C$  and  $X > Y > Z$ .

Note: The data of laser power and scanning speed are not provided due to confidentiality.



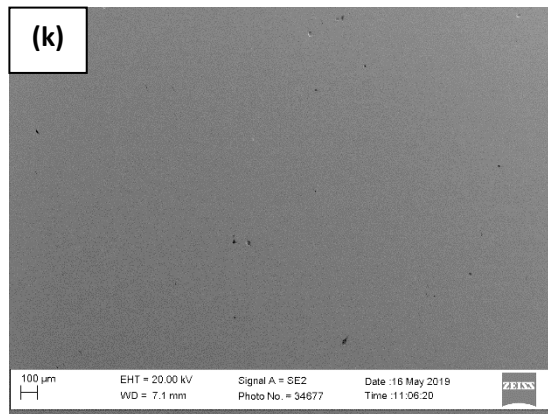
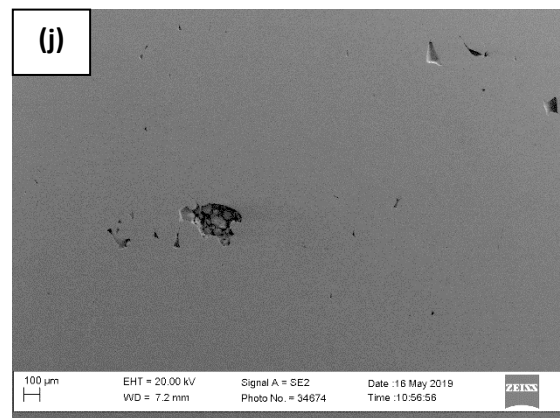
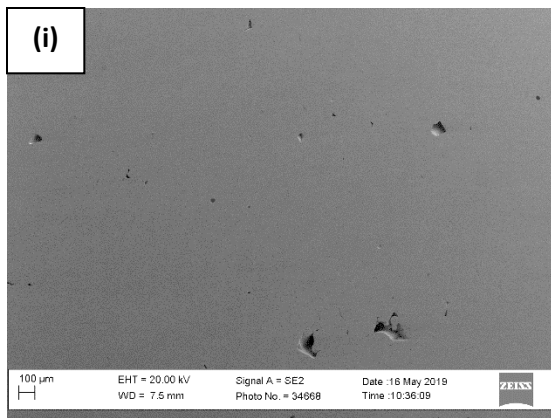
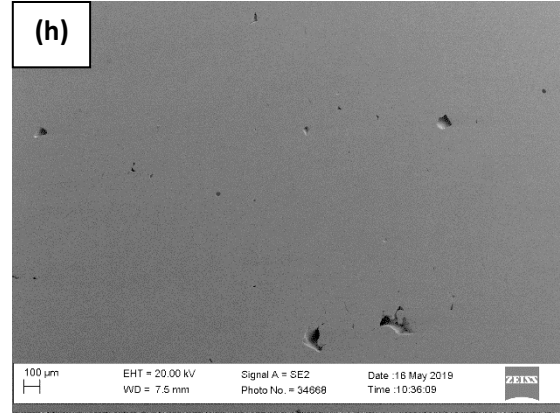
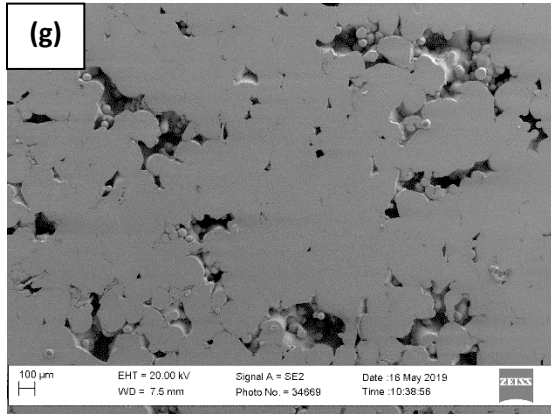


**Fig 3-3: SEM images of the samples in Table 3-1.**  
**For all SEM images: Mag = 85X, Signal A = SE2, Scan Speed = 9**

Now let's consider the melting pools in Figs 3-4, 3-5 and 3-6. It is found that the microstructure and the shape of the melting pools are related to the layer thickness (30  $\mu\text{m}$ , 45  $\mu\text{m}$  and 60  $\mu\text{m}$ ). The melting pools are well defined with 30  $\mu\text{m}$  layer thickness as shown with Fig 3-4. The microstructure produced by SLM is cellular/columnar structure which is clearer with 30  $\mu\text{m}$  layer thickness. However, this cellular/columnar structure will lose its details as the layer thickness increases to 45  $\mu\text{m}$  and 60  $\mu\text{m}$  as appeared in Figs 3-5 and 3-6. The suggested reason is as follows. For large layer thickness, the upper portion of the layer is overheated while the lower portion of the powder do not have enough heating as in the top portions. As mentioned in the introduction, this causes balling due to lack of wetting of molten pool with the preceding layer which results in a lack of fusion. In this case, big gaps are created between the layers which reduces the reheating of the old layer while melting the new one. This leads to less defined cellular structure.

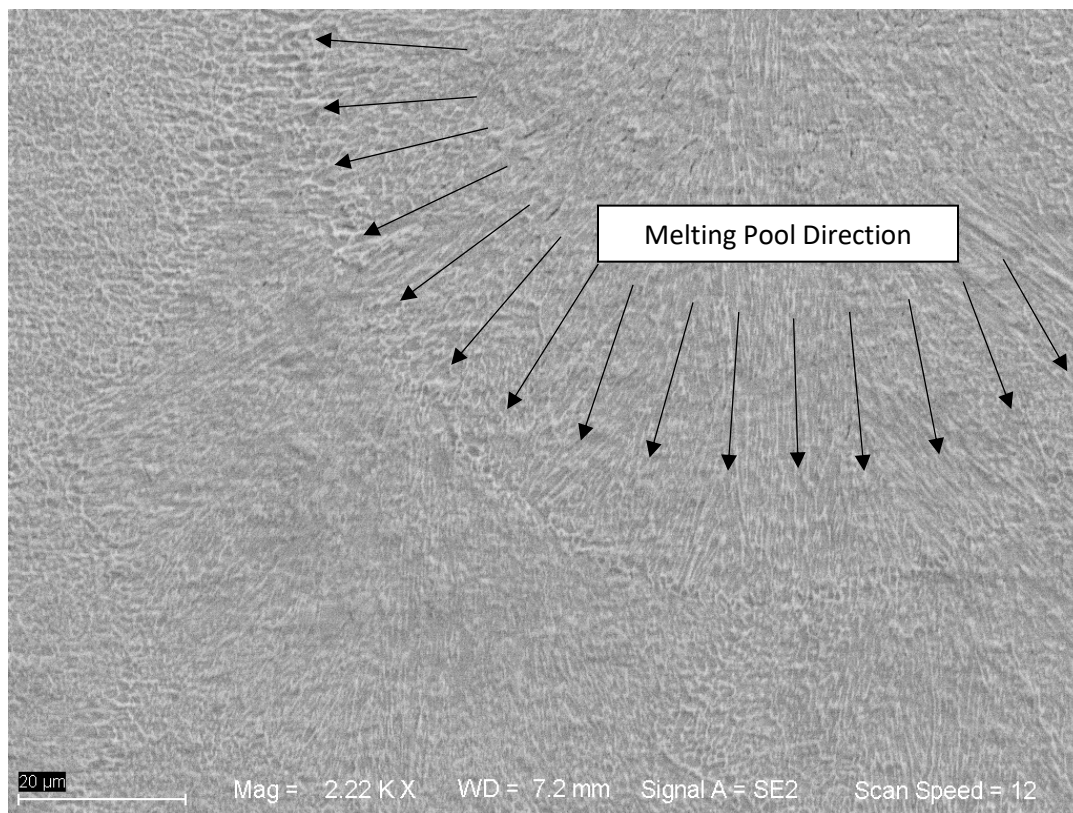


**Fig 3-4: Melting pool in sample R2 (30  $\mu\text{m}$ ).**

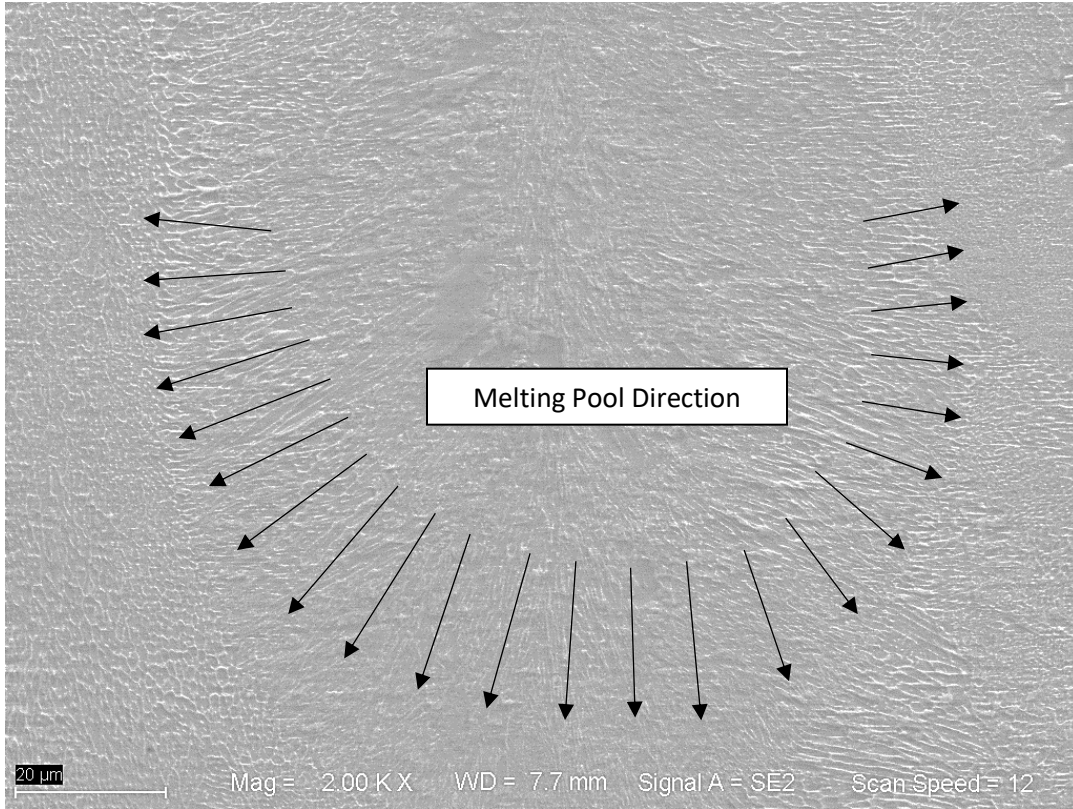


**Fig 3-5: Melting pool in sample R9 (45 μm).**

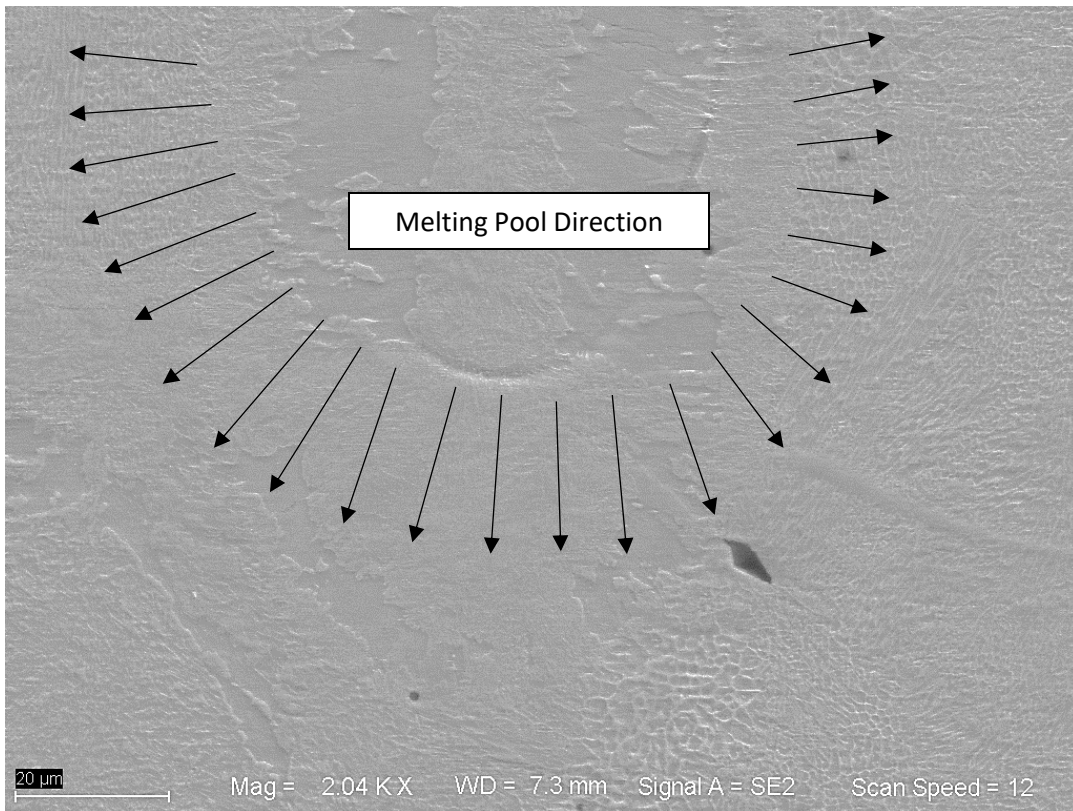


**Fig 3-6: Melting pool in sample R5 (60 μm).**

### 3.1.2 Effect of Hatch Distance

In SLM, laser spot has several scanning lines when it melts the powder, and these lines or vectors have center lines. The distance of the center lines is called “hatch distance” which indicates the spot size of the laser. With increasing or decreasing of the hatch distance, the width of laser spot will increase or decrease correspondently [28]. This leads to the fact that if the hatch distance is large, the concentration of laser spot will be less and thus the concentrated heat will be less accordingly. This will reduce the fusion of the powder. In this case, let’s take samples No. 25 and No. 29. Both samples have the same layer thickness ( $60\ \mu\text{m}$ ), laser power and scanning speed, but the hatch distance for sample No. 25 is  $0.14\ \text{mm}$  and for sample No. 29 is  $0.10\ \text{mm}$ . From Figs 3-7(a) and 3-7(b) it is shown that sample No. 25 has more defects compared to sample No. 29, because larger hatch distance affects the fusion of the material in a negative manner.

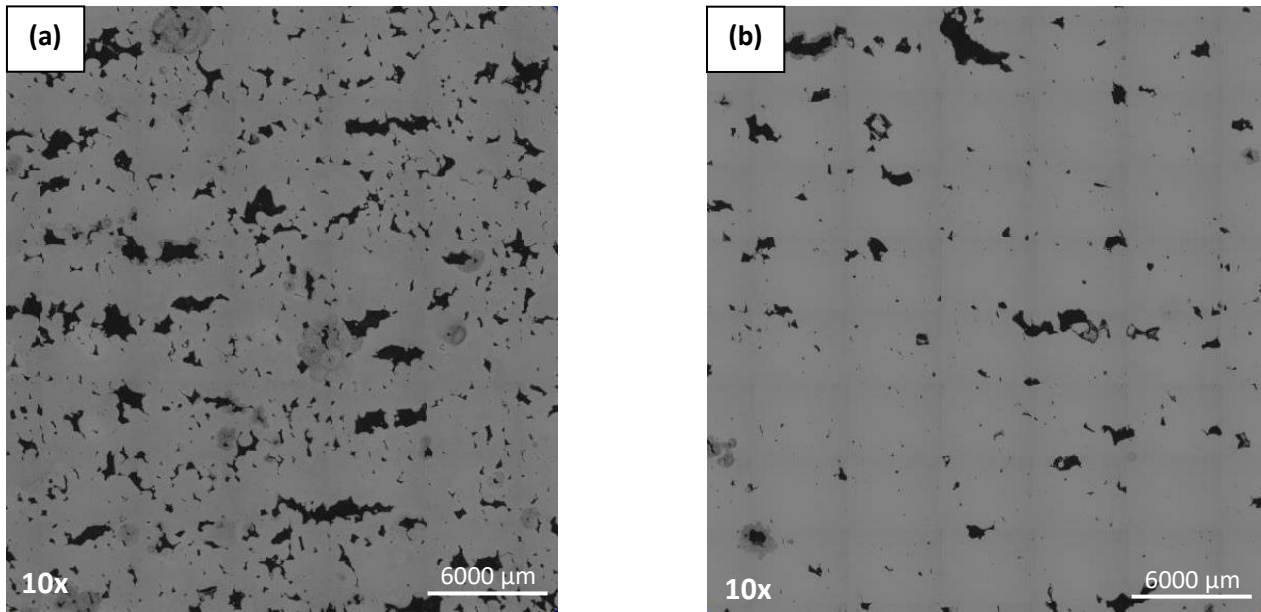


Fig 3-7: Difference in defects between different hatch distances: (a) sample No.25 ( $0.14\ \text{mm}$ ), (b) sample No.29 ( $0.10\ \text{mm}$ ).

### 3.1.3 Effect of Laser Power and Scanning Speed

Recalling equation (2), it is known that the energy density ( $E$ ) is directly proportional to laser power ( $P$ ). If the power of the laser is high enough, the powder will be melted evenly and the fusion will occur correctly. As to the speed of the scanning, the effect is opposite. Good fusion is supposed to occur at low scanning speeds. By logic, this is true, because the laser will melt each point scanned in the powder bed completely when the power of the laser is high enough and the scanning speed is low enough. As a result, the heat will be focused more on each point where the laser is scanning, leading to a good fusion for the whole layer.

As an example, let’s consider Figs 3-8, 3-9, 3-10 and 3-11, all samples have the same layer thickness ( $60\ \mu\text{m}$ ) and the same hatch distance but the laser power and the scanning speed are different. Considering samples R5 and R6, all the parameters are the same except that R5 has a laser power of  $150\ \text{W}$  and R6 has  $250\ \text{W}$ . Fig 3-9 proves that with a suitable laser power, lack of fusion will be less. Now let’s consider samples R6 and R8. They have different scanning speeds of  $650\ \text{mm/s}$  and  $900\ \text{mm/s}$  respectively, but the other three parameters are the same. Fig 3-9

confirmed that low scanning speed also reduces lack of fusion. Considering sample R7 which has 150 W and 900 mm/s, it has the largest amount of lack of fusion. Compared to samples R5, R7 and R8, sample R6 has the best combination of laser power (250 W) and scanning speed (650 mm/s). The observation confirmed the point that explained at the beginning of this paragraph.

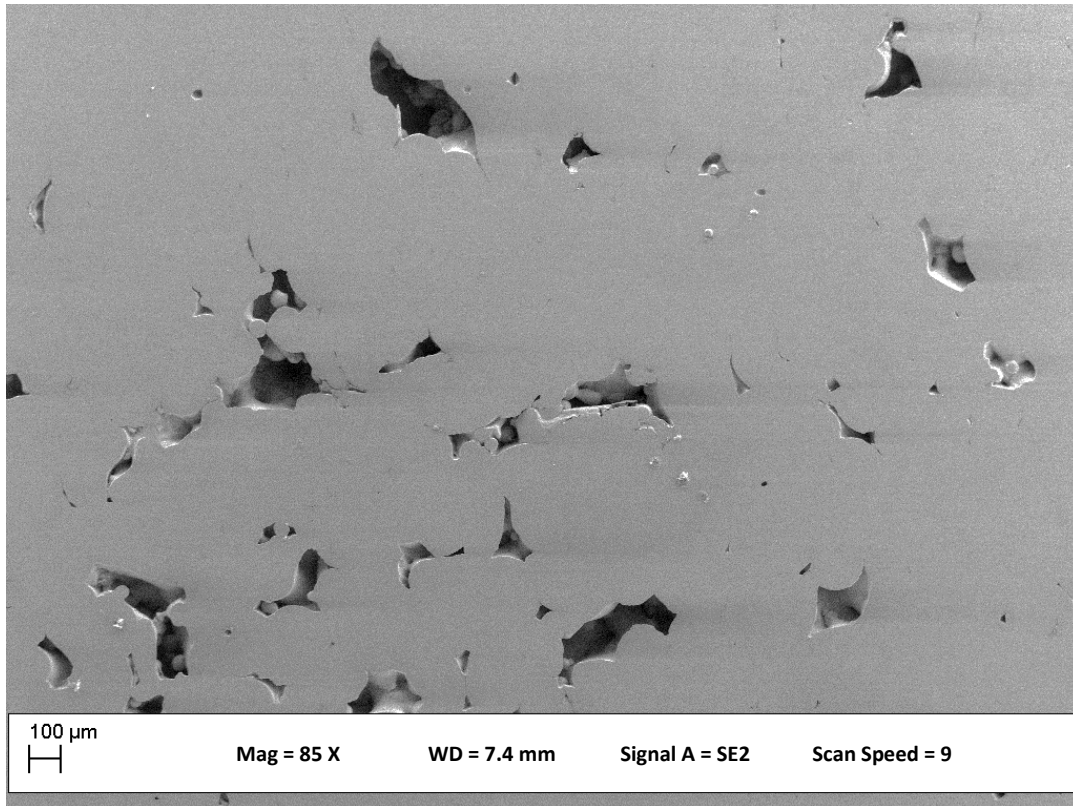


*Fig 3-8: Defects in sample R5 with laser power of 150 W and scanning speed of 650 mm/s.*

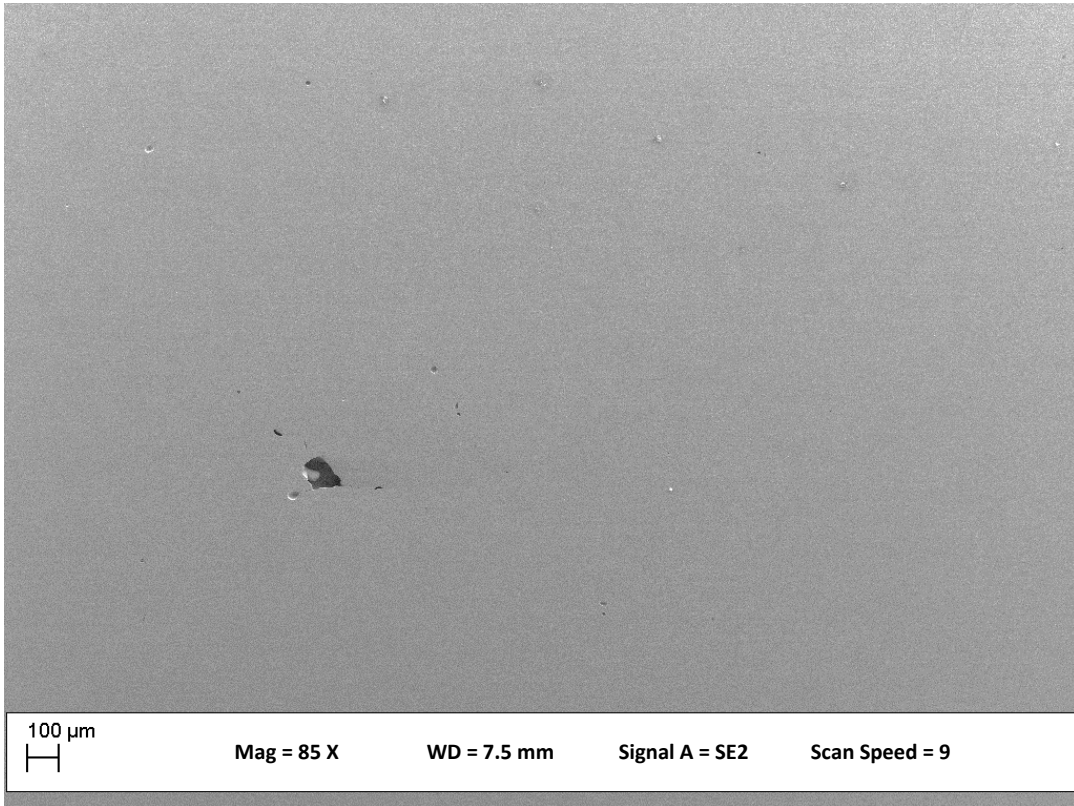


*Fig 3-9: Defects in sample R6 with laser power of 250 W and scanning speed of 650 mm/s.*

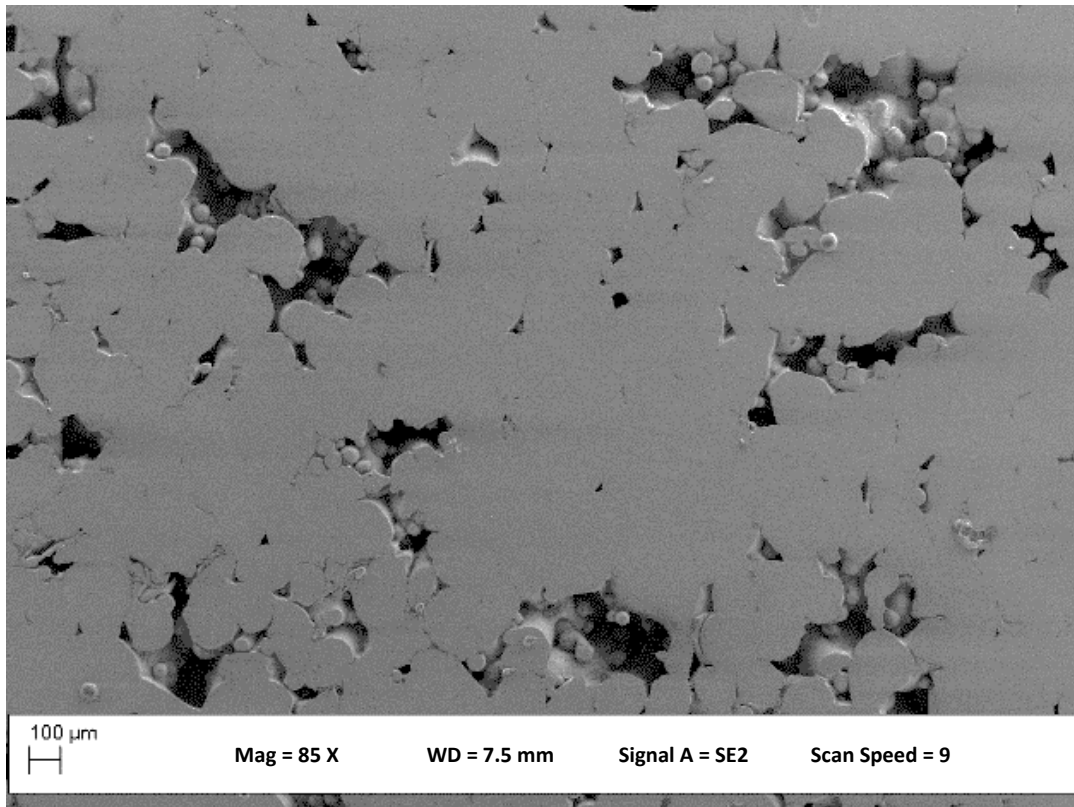


*Fig 3-10: Defects in sample R7 with laser power of 150 W and scanning speed of 900 mm/s.*

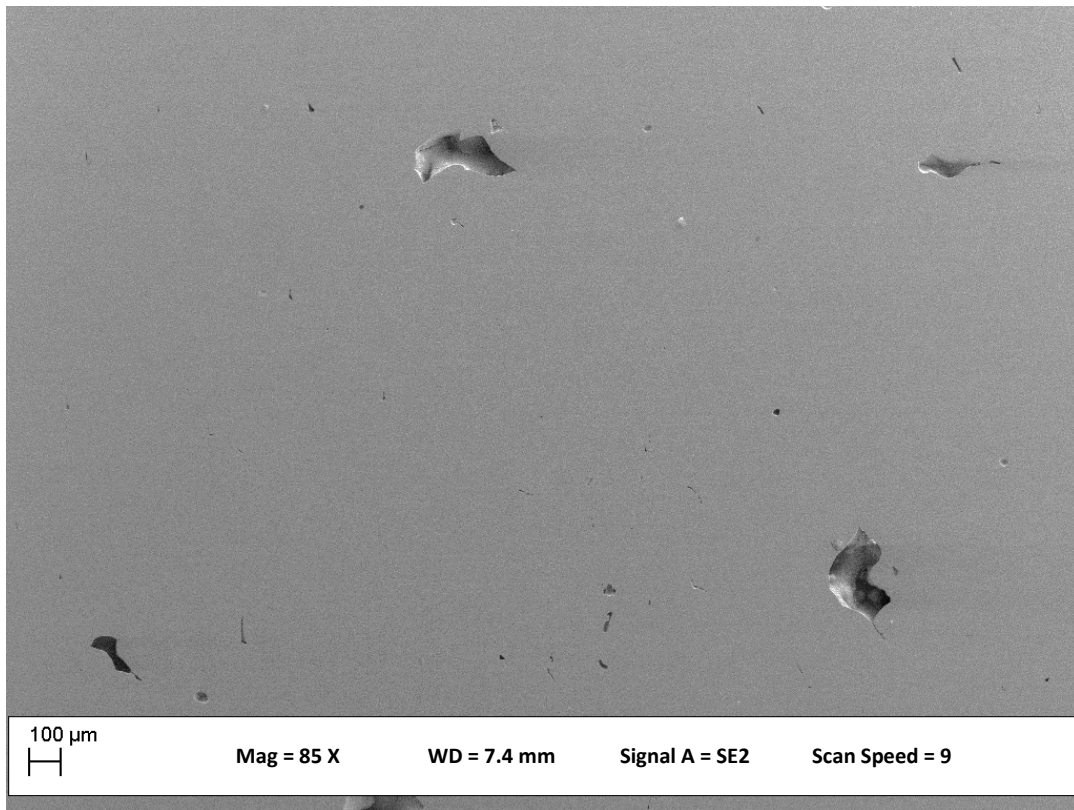


*Fig 3-11: Defects in sample R8 with laser power of 250 W and scanning speed of 900 mm/s.*

### **3.1.4 Combined Effect of Laser Power, Scanning Speed, Hatch Distance and Layer Thickness**

In previous sections, the effect of each parameter on the microstructure is studied separately. In order to have a good fusion for the powder materials, the combined effect of all four parameters should be taken into account, since energy density depends, which is the measure of the energy absorbed by the powder, on all of them. Only suitable combination of layer thickness, laser power, scanning speed and hatch distance make the fusion of the powder good enough for printing a complete functional part without much defects. By studying the effect of each parameter alone on the defects, it is found that layer thickness is so important that can control the choice of the other parameters. Choosing the layer thickness as the controller will make the choice of other parameters easier. As an example, consider a company who wants to produce a part using the same material in this research work (H13 tool steel) by means of SLM aiming at the least defects. They will go with large layer thickness ( $t$ ) of  $60\ \mu\text{m}$ . In this case the laser power ( $P$ ) should be high, the scanning speed ( $V$ ) should be low and the hatch distance ( $h$ ) should be low as well. Let's consider  $P = 300\ \text{W}$ ,  $V = 750\ \text{mm/s}$  and  $h = 0.10\ \text{mm}$ . The energy density will be:

$$E = \frac{300}{750 * 0.10 * 60 * 10^{-3}} = 66.7\ \text{[J/mm}^3\text{]}$$

Based on the references, it is found that the energy density required for H13 tool steel is approximately  $60 \text{ J/mm}^3$  depending on layer thickness [29].  $E = 66.7 \text{ J/mm}^3$  could be applicable for producing a part with density of 99.0% or above when using current printing parameters. Lack of fusion or other defects may occur if the energy density is too high or too low.

In general, it is suggested that the laser power should be high, but scanning speed and hatch distance should be low. However, it is important to keep in mind that if the layer thickness is low (say  $30 \mu\text{m}$  and below), laser power, scanning speed and hatch distance should be selected in way to avoid side effects such as extensive evaporation of the material or balling effect. This means these parameters are dependent on layer thickness to certain extent.

## **3.2 Porosity Measurements**

The porosity measurement is complementary to microstructure investigation. It is also intended to compare the average porosity sizes (based on the diameter) obtained by using two different methods. Porosity data is divided into three sets. The first set concerns the number of defects regardless if they are pores or lack of fusion, which will be used for comparing the effect of printing parameters. The second one focuses on the number of pores and the third one presents the number of lack of fusions in the microstructure. The latter two sets of data are used to compare and distinguish pores from lack of fusion.

### **3.2.1 Effect of Printing Parameters on the Number of Defects**

If other parameters are the same, in general, it is found that the number of defects (whether it is a pore or lack of fusion) increases with increasing layer thickness). Take as examples three samples, No. 01 (layer thickness:  $30 \mu\text{m}$ ), No. 21 (layer thickness:  $60 \mu\text{m}$ ) and No. 41 (layer thickness:  $45 \mu\text{m}$ ). Table 3-2 gives the number of defects with different size and the total number of defects regardless of their type. All other parameters are the same except for the layer thickness. It is discovered from Table 3-2, that sample No. 21 with  $60 \mu\text{m}$  layer thickness has the highest number of defects followed by sample No. 41. Sample No. 01 has the least number of defects. Changing layer thickness affects significantly the number of defects. It is suspected that most of the defects are lack of fusions, especially with large layer thickness (in this case  $60 \mu\text{m}$ ). The reason has been discussed before. Large layer thickness may cause incomplete fusion, leaving gaps between each layer.

Table 3-2: Comparison of the total amount of defects between different layer thicknesses.

Size Range [μm]		Total Number of Defects (Pores and Lack of fusions)		
		30 μm Layer Thickness (Sample No. 01)	60 μm Layer Thickness (Sample No. 21)	45 μm Layer Thickness (Sample No. 41)
5	10	906	2068	869
10	15	153	464	232
15	25	58	326	182
25	50	24	241	113
50	75	2	93	22
75	100	1	37	13
100		0	145	26
<b>Total</b>		1144 Defects	3374 Defects	1457 Defects

Tables 3-3, 3-4, 3-5 and 3-6 compare the number of defects from samples with different scanning speed and laser power. The samples are divided to 4 groups. The laser power and scanning speed are 150 W and 650 mm/s for Table 3-3, 250 W and 650 mm/s for Table 3-4, 150 W and 900 mm/s for Table 3-5, and 250 W and 900 mm/s for Table 3-6, respectively.

Table 3-3: Comparison of the total amount of defects between different laser power and scanning speed (first group).

Sample	Layer Thickness (μm)	Number of Defects in Each Size Range (μm) (Pores and Lack of Fusions)							
		5-10	10-15	15-25	25-50	50-75	75-100	100	Total
1	30	906	153	58	24	2	1	0	1144
21	60	2068	464	326	241	93	37	145	3374
41	45	869	232	182	113	22	13	26	1457

Table 3-4: Comparison of the total amount of defects between different laser power and scanning speed (second group).

Sample	Layer Thickness (μm)	Number of Defects in Each Size Range (μm) (Pores and Lack of Fusions)							
		5-10	10-15	15-25	25-50	50-75	75-100	100	Total
2	30	1047	204	116	56	8	2	0	1433
22	60	1483	249	120	65	10	6	5	1938
42	45	815	208	93	56	12	1	1	1186

*Table 3-5: Comparison of the total amount of defects between different laser power and scanning speed (third group).*

Sample	Layer Thickness ( $\mu\text{m}$ )	Number of Defects in Each Size Range ( $\mu\text{m}$ ) (Pores and Lack of Fusions)							
		5-10	10-15	15-25	25-50	50-75	75-100	100	Total
3	30	1005	233	126	49	2	1	0	1416
23	60	4680	1181	921	673	213	94	341	8013
43	45	1692	670	653	584	177	73	109	3958

*Table 3-6: Comparison of the total amount of defects between different laser power and scanning speed (fourth group).*

Sample	Layer Thickness ( $\mu\text{m}$ )	Number of Defects in Each Size Range ( $\mu\text{m}$ ) (Pores and Lack of Fusions)							
		5-10	10-15	15-25	25-50	50-75	75-100	100	Total
4	30	882	156	49	26	5	0	0	1118
24	60	900	178	113	88	16	10	27	1332
44	45	684	121	68	54	13	0	1	941

It is found that the number of defects will increase when having low laser power and high scanning speed as seen in Table 3-5, especially in sample No. 23 with 60  $\mu\text{m}$  layer thickness. This confirms the observation in section 3.1.3. However, if laser power and scanning speed are high, the number of defects will be low as indicated from Table 3-6. As an example, consider samples No. 44 and 43. the total defects differs by as large as 3017 by increasing the laser power from 150 W to 250 W.

For other samples in Tables 3-3 and 3-4, the story is little bit different. Both groups have low scanning speed. Increasing laser power from 150 W to 250 W makes the number of defects reduce except for 30  $\mu\text{m}$  layer thickness in which the number of defects increases with laser power slightly at low scanning speed. The reason is that an extensive evaporation of the material will occur which causes gaps or voids in the printed material. This occurs with low layer thickness, high laser power and low scanning speed. It confirms the theory in section 1.3.4. However, in Table 3-6, sample No. 44 has less defects compared to sample No. 04, indicating that this high laser power (250 W) is suitable for 45  $\mu\text{m}$  samples but is too high for 30  $\mu\text{m}$  samples.

*Table 3-7: Comparison of the total amount of defects between different hatch distances (first group). Hatch distance: 0.10 mm*

Sample	Layer Thickness ( $\mu\text{m}$ )	Number of Defects in Each Size Range ( $\mu\text{m}$ ) (Pores and Lack of fusions)							
		5-10	10-15	15-25	25-50	50-75	75-100	100	Total
1	30	906	153	58	24	2	1	0	1144
21	60	2068	464	326	241	93	37	145	3374
41	45	869	232	182	113	22	13	26	1457

*Table 3-8: Comparison of the total amount of defects between different hatch distances (second group). Hatch distance: 0.14 mm*

Sample	Layer Thickness ( $\mu\text{m}$ )	Number of Defects in Each Size Range ( $\mu\text{m}$ ) (Pores and Lack of fusions)							
		5-10	10-15	15-25	25-50	50-75	75-100	100	Total
5	30	858	281	226	175	28	7	2	1577
25	60	27456	3213	1397	780	314	160	447	33767
45	45	3274	903	683	690	279	173	216	6218

Tables 3-7 and 3-8 show the number of defects from samples with a hatch distance of 0.10 mm and 0.14 mm respectively. The readings in these Tables confirms the results from SEM and LOM. The number of defects is increased significantly when hatch distance change from 0.10 mm (Table 3-7) to 0.14 mm (Table 3-8), because hatch distance influences the focus of the laser spot on the powder bed and consequently the heat concentration.

All parameters studied play important role on the microstructure, but the dominant parameter is still the layer thickness as mentioned previously. To reduce the number of defects, in general, low layer thickness, low scanning speed and low hatch distance but high laser power are preferred. However, laser power, scanning speed and hatch distance must be selected based on the layer thickness. Too high laser power or too low scanning speed and hatch distance may cause an increase in the defects in the case of 30  $\mu\text{m}$  layer thickness as shown in Tables 3-3 to 3-6. This is consistent with the results from SEM and LOM.

### 3.2.2 Pores and Lack of Fusion

Pores and lack of fusion have different mechanisms. As mentioned in the introduction section before, pores are created as a result of gas entrapment in the material. The creation of bubbles is related to the turbulence inside the melting pool during melting. Lack of fusion occurs as a result of insufficient energy used to melt down the powder. The creation of both defects is related to laser power, scanning speed and hatch distance with the selected layer thickness.

Length to width ratio of the defects is used to define the pores and lack of fusions. The selected interval is [0.5, 1.5] for pores and [1.8, 2.5] for lack of fusions. The other intervals are not selected because the results do not show significant variation from the selected ones.

Tables 3-9 and 3-10 summarize the number of pores and lack of fusions respectively. For each layer thickness, the selected samples are divided to two groups. a) low laser power (150 W), high scanning speed (900 mm/s) and high hatch distance (0.14 mm) (samples No. 07, No. 27 and No. 47); and b) high laser power (250 W) and scanning speed (900 mm/s) with low hatch distance (0.10 mm) (samples No. 04, No. 24 and No. 44).

*Table 3-9: Number of pores for samples with different layer thickness, hatch distance, scanning speed and laser power.*

Sample	Layer Depth (µm)	Number of Pores in Each Size Range (µm)									
		0-5	5-10	10-15	15-20	20-25	25-30	30-35	35-40	40-50	Total
4	30	583	433	53	24	12	3	2	1	0	1111
7		956	1111	491	291	227	165	132	120	124	3617
24	60	638	453	106	37	22	16	14	7	8	1301
27		30348	28459	4109	1056	481	252	143	112	138	65098
44	45	453	347	63	32	21	12	6	4	1	939
47		3162	2615	752	337	255	170	152	123	219	7785

*Table 3-10: Number of lack of fusions for samples with different layer thickness, hatch distance, scanning speed and laser power.*

Sample	Layer Depth (µm)	Number of Lack of Fusions in Each Size Range (µm)									
		0-5	5-10	10-15	15-20	20-25	25-30	30-35	35-40	40-50	Total
4	30	542	433	53	24	12	4	3	1	3	1075
7		946	1111	491	291	227	167	132	121	131	3617
24	60	622	453	106	37	22	16	14	7	8	1285
27		30344	28459	4109	1056	481	252	143	112	138	65094
44	45	405	347	63	32	21	12	6	4	1	891
47		3153	2615	752	337	255	170	152	123	219	7776

From Tables 3-9 and 3-10, the number of pores and lack of fusions is very close to each other, indicating that the method used to distinguish pores from lack of fusion might be not accurate. Because it is based on trial and error, it is just an approximation.

Some useful information can be obtained when taking in the consideration the creation theory of pores and lack of fusions. For samples No. 04, No. 24 and No. 44, high laser power and scanning speed together with low hatch distance means fusion will occur in a correct manner. However, high laser power and scanning speed will cause turbulence in the melting pool in which gas bubbles will entrap and cause voids (pores).

Samples No. 07, No. 27 and No. 47 have low laser power but high scanning speed and high hatch distance. Therefore, the main defect presented in the microstructure is supposed to be lack of fusion, especially for 60 µm layer thickness as shown in Figs 3-12(a), 3-12(b) and 3-12(c). The tendency to have lack of fusion with small layer thickness is low even with 150 W laser power which is somehow suitable for 30 µm layer thickness. Mostly pores are presented in this case. As the mid value between 30 µm and 60 µm, the samples with 45 µm layer thickness probably have both defects.

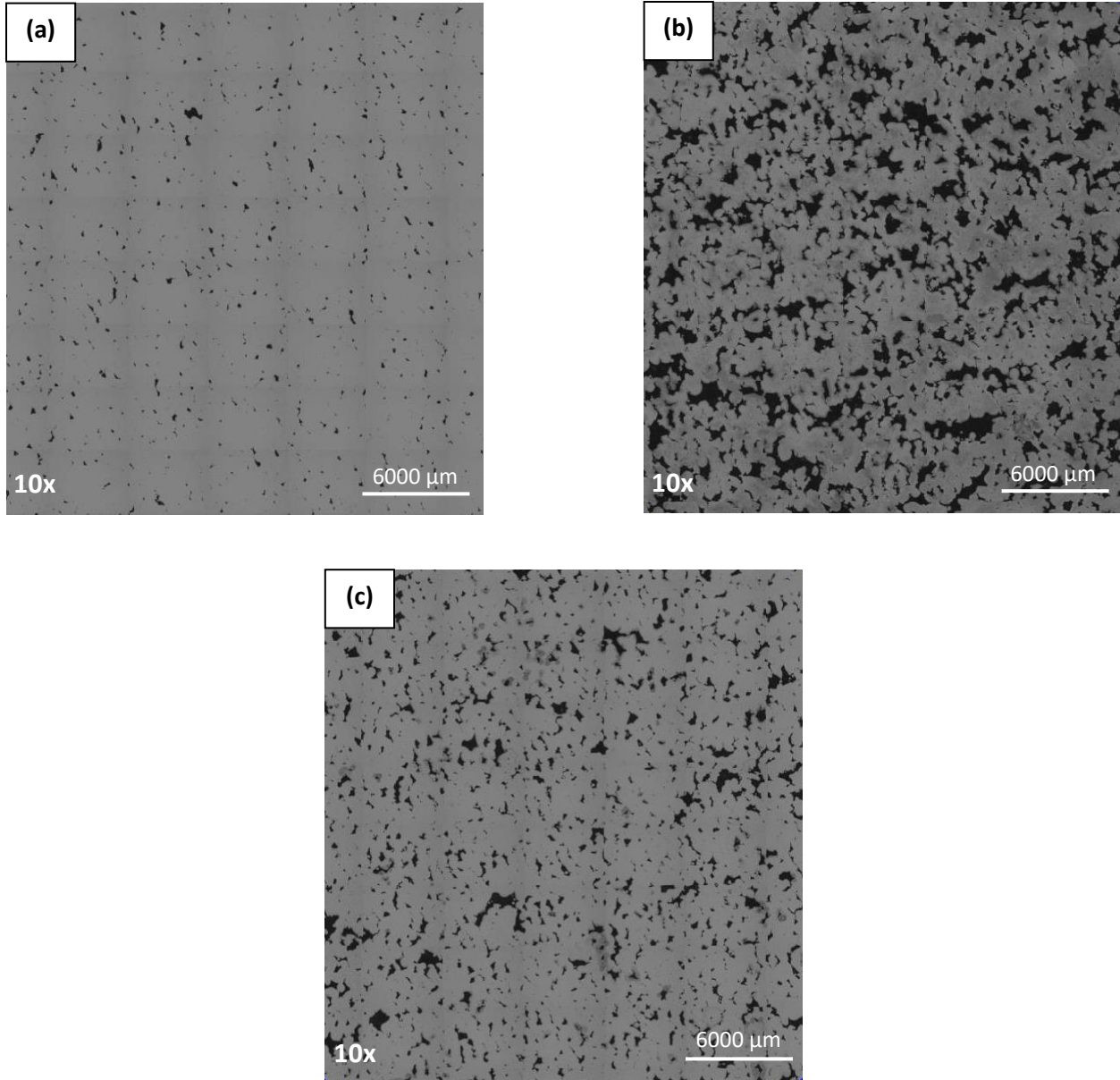


*Fig 3-12: Lack of fusions in samples (a) No. 07, (b) No. 27 and (c) No. 47. (30  $\mu\text{m}$ , 60  $\mu\text{m}$  and 45  $\mu\text{m}$  respectively).*

### **3.2.3 Average Size of Pores**

The average size of pores calculated based on the diameter is presented by Table A-2 in Appendix – A. As a general trend, the average size of pores is approximately within the similar range for the three-layer thicknesses. Consider samples No. 13 to No. 16 (30  $\mu\text{m}$ ), No. 33 to No. 36 (60  $\mu\text{m}$ ) and No. 53 to No. 56 (45  $\mu\text{m}$ ) in Table A-2. Samples No. 15 and No. 55 having low laser power and high scanning speed possesses larger average pore size. This is related to the melting pool turbulence and the entrapment of gases. As mentioned in section 1.3.4.3, low laser power and high scanning speed might cause turbulent flow since the heat concentration is not enough, leading to uneven melting and thus turbulence in the melting pool. As the turbulence increase the gas bubble will be big and consequently the pore size will be big. However, it is

difficult to explain at this stage the small average pore size from sample No. 03 (30  $\mu\text{m}$ ) and R7 (60  $\mu\text{m}$ ) and No. 35 (60  $\mu\text{m}$ ) having low laser power and high scanning speed. Another thing to note from Table A-2 is that sample No. 36 has an average pore size as large as 31.10  $\mu\text{m}$ . This pore might be created due to lack of fusion as a result of large layer thickness (60  $\mu\text{m}$ ).

The average size of the pores is normally in the range between 5  $\mu\text{m}$  and 15  $\mu\text{m}$  in diameter. This is consistent with the pore sizes between 1  $\mu\text{m}$  and 12  $\mu\text{m}$  reported by other people [30]. Notice the pores that are very close to each other could be considered as a one big pore. Although some elongated pores are observed, as seen in Fig 3-13, most length/width ratio are in the range of 1.0 to 1.5, indicating the pores can be considered approximately as circular.

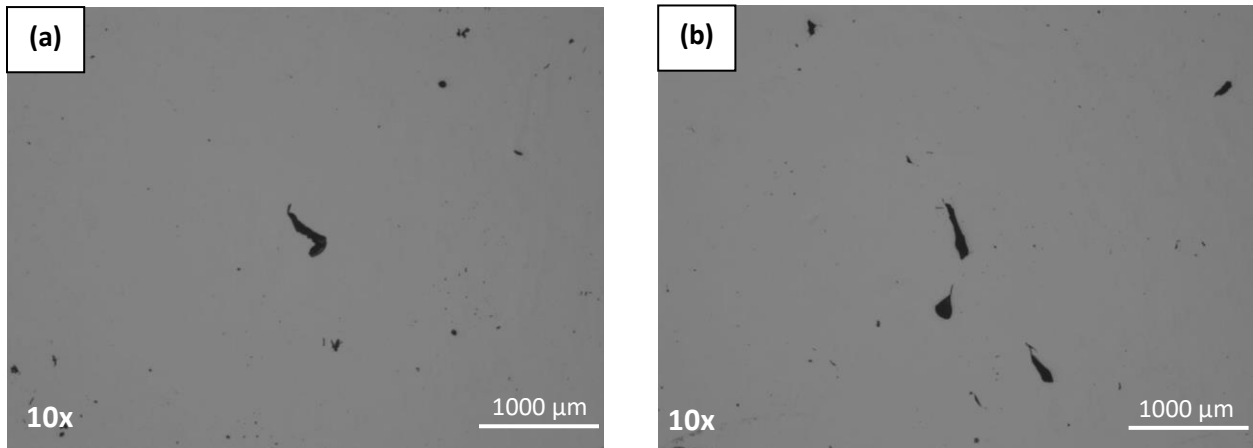


*Fig 3-13: The shape of pores in the microstructure. (a) sample R2 (30  $\mu\text{m}$ ) and (b) sample R3 (30  $\mu\text{m}$ ).*

### 3.3 Hardness

Hardness is also important to investigate the effect of SLM parameters on the microstructure. Based on previous knowledge, the hardness of tempered H13 tool steel is between 380 and 590 Vickers Hardness (HV), depending on tempering temperature which is between 200  $^{\circ}\text{C}$  and 650  $^{\circ}\text{C}$  [31].

The measured hardness of printed H13 tool steel is between 340 HV and 550 HV, which is close to the values mentioned above. However, the low hardness values are not due to conventional tempering process. It is believed that the material manufactured by SLM have a martensitic microstructure due to high cooling rates, leading to high hardness. The question arises how a low hardness is obtained before applying tempering treatment for the printed material. Fig. 3-14 shows an indentation taken on a lack of fusion for the sample R7 with 60  $\mu\text{m}$  in layer thickness. This sample has a hardness of 343.13 HV and standard deviation of 917.44 is not logical at all. R7 is one of the samples that have a lot of lack of fusion which can be seen by the naked eyes, making it hard to take hardness measurements on the surface of the sample. As a result, almost all of the hardness readings in sample R7 are not valid because most of them are taken on a defect or nearby, as shown in Fig 3-13. Distortion of the indentation can be observed sometimes

It should be mentioned that H13 tool steel produced by SLM might be self-tempered because the laser will heat the already printed layer when melting a new one. This is supposed to affect the hardness.

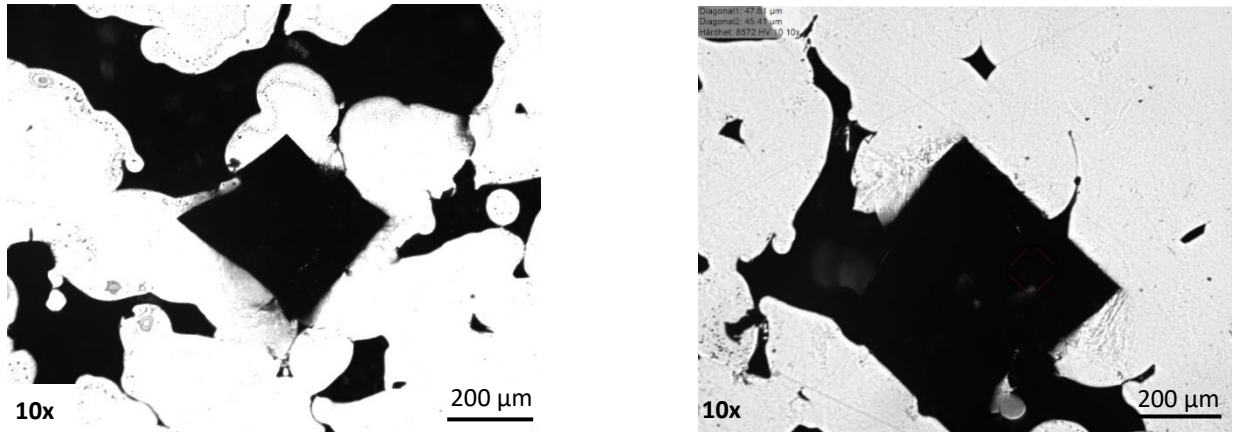


Fig 3-14: Inaccurate hardness measurements for sample R7 with 60 μm layer thickness.

### 3.3.1 Effect of Layer Thickness on Hardness

Table 3-11: Average hardness for samples with different layer thickness.

Sample	Layer Thickness (μm)	Mean Hardness (HV)	Standard Deviation
1	30	539.97	11.08
21	60	462.28	143.28
41	45	523.91	28.80

From Table A-3 in Appendix – A, the hardness measured from samples with 30 μm layer thickness is between HV 490- 570. For 45 μm and 60 μm layer thicknesses, larger deviations are observed. Samples No. 01, No. 21 and No. 41 in Table 3-11 have the same process parameters except for the layer thickness. Reasonable hardness is obtained from samples having layer thickness of 30 and 45 μm, as indicated by the small standard deviation in both samples. Increasing layer thickness to 60 μm gives rise to significantly lower hardness and larger standard deviation probably due to increased defects.

### 3.3.2 Effect of Laser Power and Scanning Speed on Hardness

Table 3-12: Average hardness for samples with different laser power and scanning speed (first group).

Sample	Layer Thickness (μm)	Mean Hardness (HV)	Standard Deviation
1	30	539.97	11.08
21	60	462.28	143.28
41	45	523.91	28.80

Table 3-13: Average hardness values for samples with different laser power and scanning speed (second group).

Sample	Layer Thickness (μm)	Mean Hardness (HV)	Standard Deviation
2	30	570.10	13.90
22	60	545.20	20.39
42	45	553.63	17.47

*Table 3-14: Average hardness values for samples with different laser power and scanning speed (third group).*

Sample	Layer Thickness (µm)	Mean Hardness (HV)	Standard Deviation
3	30	535.18	8.49
23	60	345.44	180.05
43	45	495.29	76.15

*Table 3-15: Average hardness values for samples with different laser power and scanning speed (fourth group).*

Sample	Layer Thickness (µm)	Mean Hardness (HV)	Standard Deviation
4	30	552.63	15.28
24	60	528.60	52.68
44	45	538.99	59.19

The hardness is also affected by laser power and scanning speed. With high laser power and low scanning speed, the fusion of the material is good. Less defects makes the hardness high and accurate. Considering samples in Table 3-13, the hardness for samples No. 02, No. 22 and No. 42 are the maximum because of their high laser power of 250 W and low scanning speed of 650 mm/s. Samples No. 03, No. 23 and No. 43 having laser power of 150 W and scanning speed of 900 mm/s, on the other hand, possess the smallest hardness among all the samples in the group (Table 3-14). Less concentration of laser spot due to the increment of scanning speed (900 mm/s) will decrease the focus of the heat in the scanning spot and consequently reduces the fusion of the material. Mid values of hardness are obtained either with small laser power and scanning speed (150 W and 650 mm/s) in Tables 3-12 or with large laser power and scanning speed (250 W and 900 mm/s) in Table 3-15. In these cases, low laser power is compensated by low scanning speed or the high scanning speed is compensated by the high laser power. The laser will have time to melt the material. Consequently, the material will be melted in a relatively good manner and hence mid hardness are obtained.

### 3.3.3 Effect of Hatch Distance on Hardness

*Table 3-16: Average hardness for samples with different hatch distance (first group).*

Sample	Layer Thickness (µm)	Mean Hardness (HV)	Standard Deviation
1	30	539.97	11.08
21	60	462.28	143.28
41	45	523.91	28.80

*Table 3-17: Average hardness for samples with different hatch distance (second group).*

Sample	Layer Thickness (µm)	Mean Hardness (HV)	Standard Deviation
5	30	533.66	10.34
25	60	358.20	160.30
45	45	451.94	132.35

The hatch distance is 0.10 mm in Table 3-16 and 0.14 in Table 3-17. As hatch distance increases, defects will increase, as discussed previously. This affects hardness of the material negatively.

The hardness results are consistent with the observation from SEM, LOM and porosity measurements. Small layer thickness, high laser power, low scanning speed and low hatch distance are important in order to have a good or optimized printed part.

### 3.3.4 Average Hardness Along Building Direction

It is generally believed that the properties of the SLM produced part will have a variation in building (printing) direction. To prove that, average hardness along the x-axis and along the z-axis (printing direction) are measured. It is found that there is no significant variation along the x-axis. The variation occurs mostly along the printing direction since the defects especially lack of fusion appears between the printed layers. Table 3-18 compares the average hardness in the printing direction from top to bottom for three samples with different layer thickness.

Table 3-18: Average hardness in z-axis (building direction).

Sample No. 04 (30 $\mu\text{m}$ Layer Thickness)		Sample No. 24 (60 $\mu\text{m}$ Layer Thickness)		Sample No. 44 (45 $\mu\text{m}$ Layer Thickness)	
Mean Hardness (HV)	Standard Deviation	Mean Hardness (HV)	Standard Deviation	Mean Hardness (HV)	Standard Deviation
570.80	12.28	551.10	6.24	564.60	8.22
562.50	13.58	<b>501.10</b>	<b>114.48</b>	556.20	9.77
556.20	9.44	541.80	10.28	<b>492.20</b>	<b>173.58</b>
551.70	13.09	527.80	34.16	540.60	10.94
548.60	13.73	532.10	25.89	540.80	10.63
542.40	12.99	538.60	10.55	544.20	8.60
550.90	12.36	530.80	16.56	533.90	12.84
543.40	13.55	504.00	96.89	541.80	13.16
547.20	16.25	530.10	13.40	536.60	11.60

The hardness in the table does not follow any specific order and changes randomly. This is probably related to the appearance of defects. Meanwhile, the errors in hardness readings will increase with the layer thickness, as shown by the standard deviation for samples No. 24 and No. 44. Most of high average hardness values are connected to sample No. 04 which has small layer thickness. This confirms that with proper printing parameters the defects between layers will be less, thus, the hardness will be within the normal range for H13 tool steel.

## 3.4 Density

As layer thickness increases the density decreases, as indicated in Table 3-19. It is known that the density is directly proportional to the mass of the cube with fixed dimensions. The samples with 60  $\mu\text{m}$  in layer thickness having a lot of pores and lack of fusions will decrease the mass of the cube and consequently the density. The density ratios of the printed samples and the raw material are in the range of 98.38% to 99.94%, 90.52% to 99.93% and 83.47% to 99.71% when the layer thickness is 30, 45 and 60  $\mu\text{m}$  respectively. The decrease in the ratio for 60  $\mu\text{m}$  layer thickness confirms the existence of voids, pores and lack of fusions which leads to reduced density as shown in Table A-1 in Appendix – A.

The effect of laser power on the density is dependent on layer thickness. Consider 3 sample groups: No. 01 and No. 02 with 30  $\mu\text{m}$  layer thickness, No. 21 and No. 22 with 60  $\mu\text{m}$  layer

thickness and No. 41 and No. 42 with 45  $\mu\text{m}$  layer thickness. The two samples in each layer thickness group have a difference of 100 W in laser power. With 30  $\mu\text{m}$  and 45  $\mu\text{m}$  layer thickness, the density ratio keeps almost unchanged. The small variation can be some sort of error due to measurement. For samples with 60  $\mu\text{m}$  layer thickness, the ratio increased with increasing laser power from sample No. 21 and No. 22. The reason is that the fusion will be good with high laser power, leading to less defects and consequently higher density.

The same story occurs for scanning speed. Consider samples No. 01 and No. 03 with 30  $\mu\text{m}$  layer thickness, No. 21 and No. 23 with 60  $\mu\text{m}$  layer thickness and No. 41 and No. 43 with 45  $\mu\text{m}$  layer thickness. The two samples in each layer thickness group have a difference of 250 mm/s in scanning speed. For 30  $\mu\text{m}$  layer thickness, the density ratio keeps almost unchanged. For samples with 60  $\mu\text{m}$  and 45  $\mu\text{m}$  layer thickness, the behavior is different. The density ratio decreased with increasing scanning speed. The reason is that the fusion will be less with high scanning speed, giving rise to increased defects and therefore lower density.

As to the effect of hatch distance, consider samples No. 01 and No. 05 with 30  $\mu\text{m}$  layer thickness, No. 21 and No. 25 with 60  $\mu\text{m}$  layer thickness and No. 41 and No. 45 with 45  $\mu\text{m}$  layer thickness. The two samples in each thickness group have a difference of 0.04 mm in hatch distance. Change of the hatch distance causes the same behavior on the density as changing scanning speed due to similar reasons.

*Table 3-19: Density ratios of the printed samples to the raw powder material.*

<b>Samples 30 <math>\mu\text{m}</math> Layer Thickness</b>	<b>Density Ratio (%)</b>	<b>Samples 60 <math>\mu\text{m}</math> Layer Thickness</b>	<b>Density Ratio (%)</b>	<b>Samples 45 <math>\mu\text{m}</math> Layer Thickness</b>	<b>Density Ratio (%)</b>
<b>1</b>	99.69	<b>21</b>	96.27	<b>41</b>	99.65
<b>2</b>	99.21	<b>22</b>	99.54	<b>42</b>	99.53
<b>3</b>	99.73	<b>23</b>	92.45	<b>43</b>	98.20
<b>5</b>	99.87	<b>25</b>	91.86	<b>45</b>	97.81

H13 tool steel is a hard material having high carbon content. Formation of very hard and stable carbides with other alloying elements such as vanadium makes the fusion of the material difficult especially when parameters in a SLM process are not improper. Based on the results from SEM/LOM, porosity measurements, hardness measurements and density ratios, it has been found that all parameters investigated have a large influence on the microstructure of H13 tool steel. However, layer thickness is the dominant parameter because in industry the production rate is important. The selection of laser power, scanning speed and hatch distance is based on layer thickness.

To have less defects for H13 tool steel produced by SLM, laser power should be high, scanning speed and hatch distance should be low for 60  $\mu\text{m}$  and 45  $\mu\text{m}$  layer thicknesses. However, for 30  $\mu\text{m}$  layer thickness, laser power and scanning speed should be high and hatch distance should be low.

### 3.5 Preliminary information of Chemical Composition

Regarding the chemical composition, EDS analysis shows that there is a negligible segregation of alloying elements such as manganese (Mn) and vanadium (V). The analyzed places and the corresponding concentration of elements with the standard deviation are shown in Fig 3-15 and Table 3-20 respectively. For R2 sample (30  $\mu\text{m}$  in layer thickness), the concentration of vanadium and manganese is between 1.0 wt% to 1.2 and 0.3-0.5 wt% respectively. It should be mentioned that the EDS measurements are not accurate for carbon.

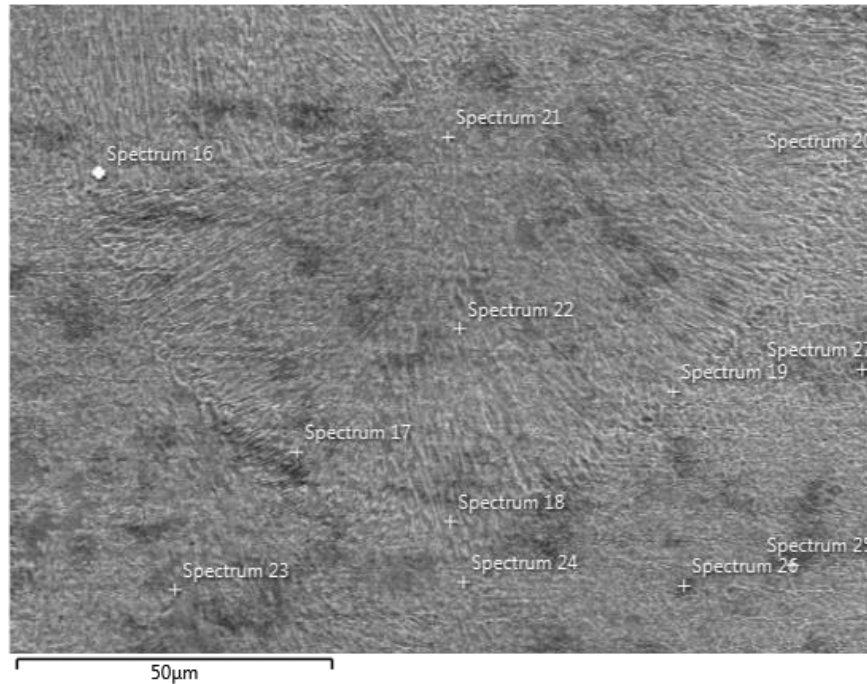


Fig 3-15: Location of EDX analysis on sample R2.

Table 3-20: Chemical composition at different locations in sample R2 (wt%).

Spectrum	Fe	C	Cr	Mo	V	Si	Mn
16	86.8	3.7	5.5	1.6	1.2	0.9	0.3
17	85.5	5.0	5.5	1.6	1.2	0.9	0.4
18	86.4	4.4	5.5	1.5	1.1	0.8	0.4
19	84.1	6.2	5.4	1.8	1.2	0.9	0.4
20	87.6	3.5	5.3	1.3	1.1	0.8	0.4
21	85.1	5.6	5.3	1.7	1.1	0.9	0.4
22	86.7	3.7	5.5	1.6	1.2	0.8	0.5
23	86.9	3.8	5.5	1.5	1.1	0.8	0.4
24	86.3	4.7	5.3	1.4	1.1	0.8	0.4
25	85.2	5.6	5.4	1.5	1.1	0.8	0.5
26	84.5	6.4	5.3	1.5	1.1	0.8	0.4
27	80.3	11.2	5.1	1.3	1.0	0.8	0.3

# CHAPTER 4

## Conclusion and Remarks

H13 is one of the hard-to-build materials and it is difficult to print without having problems in the microstructure because its high carbon content causes the formation of hard alloy carbides which are difficult to be melted during SLM process.

It is concluded that the layer thickness is the governing parameter. And it can be used as a controller for other parameters. In order to obtain high hardness, high density and low porosity within 30  $\mu\text{m}$ , 45  $\mu\text{m}$  and 60  $\mu\text{m}$  layer thicknesses, it is in general important to have:

- High laser power.
- Low scanning speed.
- Low hatch distance.

The optimization of the parameters is decided by the layer thickness. For small layer thickness, defects can present in the microstructure if laser power is too high, scanning speed is too low and hatch distance is too low. All the parameters should have good correlation with each other.

Parameter optimization of the SLM process is a wide field and needs a lot of research in order to obtain high quality products. It is not enough only to optimize printing parameters that influence energy density. Consideration of other parameters such as cooling rates control, preheating temperatures, position and orientation of the build and so on are of importance since they may have large influences on the mechanical properties and microstructure of the material.

# CHAPTER 5

## **Future Work**

There are several topics of interest regarding optimization of SLM process parameters for H13:

- To conduct more studies on the mechanical properties of H13 tool steel produced by SLM.
- To study the effect of preheating and controlled cooling for SLM of H13 tool steel and compare with that at room temperature.
- To apply the optimized parameters obtained from simple geometries to more complex geometries and compare.

# References

- [1] Böckin, D., & Tillman, A. M. (2019). Environmental assessment of additive manufacturing in the automotive industry. *Journal of Cleaner Production*, 226, 977–987. <https://doi.org/10.1016/j.jclepro.2019.04.086>
- [2] Fredriksson, C. (2019). Sustainability of metal powder additive manufacturing. *Procedia Manufacturing*, 33, 139–144. <https://doi.org/10.1016/j.promfg.2019.04.018>
- [3] Nakazawa, Y. Tamura, K. Yoshida, M. Takagi, K. Kano, M. (2005). Development of crash-box for passenger car with high capability for energy absorption. Sumitomo Metal Industries.
- [4] ASTM INTERNATIONAL. (2013). ASTM F2792-12a. *Rapid Manufacturing Association*, 1–3. <https://doi.org/10.1520/F2792-12A.2>
- [5] Rashid, A. (2019). *Additive Manufacturing Technologies*. *CIRP Encyclopedia of Production Engineering*. [https://doi.org/10.1007/978-3-662-53120-4\\_16866](https://doi.org/10.1007/978-3-662-53120-4_16866)
- [6] Lee, H., Lim, C. H. J., Low, M. J., Tham, N., Murukeshan, V. M., & Kim, Y. J. (2017). Lasers in additive manufacturing: A review. *International Journal of Precision Engineering and Manufacturing - Green Technology*, 4(3), 307–322. <https://doi.org/10.1007/s40684-017-0037-7>
- [7] Lee, J. H., Jang, J. H., Joo, B. D., Yim, H. S., & Moon, Y. H. (2009). Application of direct laser metal tooling for AISI H13 tool steel. *Transactions of Nonferrous Metals Society of China (English Edition)*, 19(SUPPL. 1), s284–s287. [https://doi.org/10.1016/S1003-6326\(10\)60286-5](https://doi.org/10.1016/S1003-6326(10)60286-5)
- [8] Kurzynowski, T., Chlebus, E., Kuźnicka, B., & Reiner, J. (2012). Parameters in selective laser melting for processing metallic powders. *High Power Laser Materials Processing: Lasers, Beam Delivery, Diagnostics, and Applications*, 8239(February), 823914. <https://doi.org/10.1117/12.907292>
- [9] Yap, C. Y., Chua, C. K., Dong, Z. L., Liu, Z. H., Zhang, D. Q., Loh, L. E., & Sing, S. L. (2015). Review of selective laser melting: Materials and applications. *Applied Physics Reviews*, 2(4). <https://doi.org/10.1063/1.4935926>
- [10] Kruth, J. P., Badrossamay, M., Yasa, E., Deckers, J., Thijs, L., & Van Humbeeck, J. (2010). Part and material properties in selective laser melting of metals. *16th International Symposium on Electromachining, ISEM 2010*, (January 2015), 3–14.
- [11] Olakanmi, E. O., Cochrane, R. F., & Dalgarno, K. W. (2015). A review on selective laser sintering/melting (SLS/SLM) of aluminium alloy powders: Processing, microstructure, and properties. *Progress in Materials Science*, 74, 401–477. <https://doi.org/10.1016/j.pmatsci.2015.03.002>
- [12] A. Handbook, “Properties and selection: irons, steels, and high-performance alloys,” ASM Int., 1990.
- [13] Højerslev, C. (2001). Tool steels, 493–494.
- [14] Pinnow, K. E., Stasko, W., & Corporation, C. M. (2018). P/M Tool Steels. *Properties and Selection: Irons, Steels, and High-Performance Alloys*, 1, 780–792. <https://doi.org/10.31399/asm.hb.v01.a0001042>
- [15] 2004, W. by A. Z. M. M. 29. (2017, August 1). Tool Steels - Heat Treatment Considerations for Water, Oil and Air Hardening Tool Steels. Retrieved from <https://www.azom.com/article.aspx?ArticleID=2445>.

- [16] Britannica, T. E. of E. (n.d.). Tempering. Retrieved October 14, 2019, from <https://www.britannica.com/technology/tempering-metallurgy>.
- [17] Beiss, P. (2018). Properties of Powder Metallurgy Tool Steels. *Powder Metallurgy*, 7, 491–514. <https://doi.org/10.31399/asm.hb.v07.a0006127>
- [18] Beiss, P. (2018). Microstructure of Powder Metallurgy Tool Steels. *Powder Metallurgy*, 7, 533–535. <https://doi.org/10.31399/asm.hb.v07.a0006131>
- [19] Bayer, A. M., Becherer, B. a, & Vasco, T. (1989). High Speed Tool Steels, *16*(Ref 2), 51–59.
- [20] Steel, H. S., & Data, T. (2019). H13 T, 2–4.
- [21] Badrossamay, M., & Childs, T. H. C. (2007). Further studies in selective laser melting of stainless and tool steel powders. *International Journal of Machine Tools and Manufacture*, 47(5 SPEC. ISS.), 779–784. <https://doi.org/10.1016/j.ijmachtools.2006.09.013>
- [22] Guan, K., Wang, Z., Gao, M., Li, X., & Zeng, X. (2013). Effects of processing parameters on tensile properties of selective laser melted 304 stainless steel. *Materials and Design*, 50, 581–586. <https://doi.org/10.1016/j.matdes.2013.03.056>
- [23] Joseph I. Goldstein et al., *Scanning Electron Microscopy and X-Ray Microanalysis*, Springer 2003
- [24] Joseph Goldstein (2003). *Scanning Electron Microscopy and X-Ray Microanalysis*. Springer. ISBN 978-0-306-47292-3. Retrieved 18 March 2018.
- [25] My Scopetraining for advanced research. (n.d.). Retrieved March 19, 2018, from <http://www.ammrf.org.au/myscope/analysis/eds/xraydetection/>
- [26] Acott, Chris (1999). "The diving "Law-ers": A brief resume of their lives". *South Pacific Underwater Medicine Society Journal*. 29 (1). ISSN 0813-1988. OCLC 16986801. Retrieved 2009-06-13.
- [27] Simchi, A., & Pohl, H. (2003). Effects of laser sintering processing parameters on the microstructure and densification of iron powder. *Materials Science and Engineering A*, 359(1–2), 119–128. [https://doi.org/10.1016/S0921-5093\(03\)00341-1](https://doi.org/10.1016/S0921-5093(03)00341-1)
- [28] Processing, C. M. (2019). Journals & Books Create account Sign in 10 . 01 - Introduction to Advances in Additive Manufacturing and Tooling, (12), 1–2.
- [29] Narvan, M., Al-Rubaie, K. S., & Elbestawi, M. (2019). Process-Structure-Property Relationships of AISI H13 Tool Steel Processed with Selective Laser Melting. *Materials*, 12(14), 2284. doi: 10.3390/ma12142284
- [30] Slotwinski, J. A., Garboczi, E. J., & Hebenstreit, K. M. (2014). Porosity Measurements and Analysis for Metal Additive Manufacturing Process Control. *Journal of Research of the National Institute of Standards and Technology*, 119, 494. doi: 10.6028/jres.119.019
- [31] Sohn, K. Y., Allison, S. A., & Johns, J. W. (n.d.). Manganese containing inclusions in LPDC AM50 alloys. *Magnesium Technology 2000*, (815), 50–52.

# Appendix – A

Table A-1: Density ratios between the printed samples and the original density of the powder material.

Samples 30 $\mu$ m Layer Thickness	Density Ratio (%)	Samples 60 $\mu$ m Layer Thickness	Density Ratio (%)	Samples 45 $\mu$ m Layer Thickness	Density Ratio (%)
<b>R1</b>	99.96	<b>R5</b>	93.85	<b>R9</b>	99.23
<b>R2</b>	99.80	<b>R6</b>	99.89	<b>R10</b>	99.39
<b>R3</b>	99.61	<b>R7</b>	86.67	<b>R11</b>	99.82
<b>R4</b>	99.76	<b>R8</b>	98.48	-	-
<b>1</b>	99.69	<b>21</b>	96.27	<b>41</b>	99.65
<b>2</b>	99.21	<b>22</b>	99.54	<b>42</b>	99.53
<b>3</b>	99.73	<b>23</b>	92.45	<b>43</b>	98.20
<b>4</b>	99.73	<b>24</b>	99.40	<b>44</b>	99.77
<b>5</b>	99.87	<b>25</b>	91.86	<b>45</b>	97.81
<b>6</b>	99.71	<b>26</b>	99.54	<b>46</b>	99.66
<b>7</b>	98.38	<b>27</b>	84.06	<b>47</b>	91.97
<b>8</b>	99.69	<b>28</b>	96.16	<b>48</b>	98.81
<b>9</b>	99.73	<b>29</b>	96.70	<b>49</b>	99.89
<b>10</b>	99.41	<b>30</b>	99.66	<b>50</b>	99.46
<b>11</b>	99.72	<b>31</b>	91.07	<b>51</b>	98.79
<b>12</b>	99.70	<b>32</b>	99.47	<b>52</b>	99.83
<b>13</b>	99.77	<b>33</b>	91.64	<b>53</b>	97.61
<b>14</b>	99.85	<b>34</b>	99.71	<b>54</b>	99.92
<b>15</b>	98.42	<b>35</b>	83.47	<b>55</b>	90.52
<b>16</b>	99.68	<b>36</b>	96.26	<b>56</b>	99.54
<b>17</b>	99.76	<b>37</b>	97.38	<b>57</b>	99.69
<b>18</b>	99.69	<b>38</b>	96.53	<b>58</b>	99.51
<b>19</b>	99.66	<b>39</b>	96.73	<b>59</b>	99.72
<b>20</b>	99.94	<b>40</b>	99.54	<b>60</b>	99.93

Table A-2: Pores average size for all the samples.

Samples 30 $\mu\text{m}$ Layer Thickness	Mean Size ( $\mu\text{m}$ )	Samples 60 $\mu\text{m}$ Layer Thickness	Mean Size ( $\mu\text{m}$ )	Samples 45 $\mu\text{m}$ Layer Thickness	Mean Size ( $\mu\text{m}$ )
<b>R1</b>	8.1	<b>R5</b>	9.1	<b>R9</b>	8.2
<b>R2</b>	8.5	<b>R6</b>	7.3	<b>R10</b>	8.0
<b>R3</b>	10.0	<b>R7</b>	8.2	<b>R11</b>	7.8
<b>R4</b>	8.4	<b>R8</b>	9.0	-	-
<b>1</b>	8.10	<b>21</b>	10.40	<b>41</b>	10.30
<b>2</b>	8.90	<b>22</b>	8.30	<b>42</b>	9.30
<b>3</b>	5.00	<b>23</b>	10.40	<b>43</b>	12.20
<b>4</b>	8.10	<b>24</b>	9.40	<b>44</b>	9.20
<b>5</b>	10.30	<b>25</b>	7.20	<b>45</b>	11.70
<b>6</b>	8.30	<b>26</b>	11.10	<b>46</b>	8.50
<b>7</b>	15.20	<b>27</b>	8.50	<b>47</b>	11.80
<b>8</b>	9.40	<b>28</b>	10.40	<b>48</b>	10.50
<b>9</b>	8.60	<b>29</b>	11.10	<b>49</b>	8.40
<b>10</b>	9.30	<b>30</b>	9.60	<b>50</b>	8.10
<b>11</b>	8.70	<b>31</b>	8.20	<b>51</b>	10.10
<b>12</b>	8.50	<b>32</b>	9.10	<b>52</b>	7.60
<b>13</b>	10.00	<b>33</b>	13.30	<b>53</b>	12.90
<b>14</b>	9.00	<b>34</b>	10.90	<b>54</b>	9.20
<b>15</b>	14.90	<b>35</b>	10.10	<b>55</b>	12.90
<b>16</b>	9.40	<b>36</b>	31.10	<b>56</b>	11.50
<b>17</b>	8.30	<b>37</b>	10.80	<b>57</b>	8.50
<b>18</b>	8.90	<b>38</b>	12.30	<b>58</b>	9.50
<b>19</b>	8.50	<b>39</b>	9.90	<b>59</b>	9.20
<b>20</b>	8.40	<b>40</b>	8.60	<b>60</b>	8.40

The calculations of average pore size are performed as follows:

1. The pores are sorted according to the sizes or diameters calculated from the software (Leica): 5  $\mu\text{m}$ , 10  $\mu\text{m}$ , 15  $\mu\text{m}$ , 20  $\mu\text{m}$ , 25  $\mu\text{m}$ , 30  $\mu\text{m}$ , 35  $\mu\text{m}$ , 40  $\mu\text{m}$ , 45  $\mu\text{m}$  and 50  $\mu\text{m}$ .
2. The frequency function in Excel is used to find the number of pores in each size.
3. The sum of the products of the pore number and the corresponding diameter is taken
4. The value obtained in step 3 is divided by the total number of pores to find the average size of pores.

Table A-3: Mean hardness values for all the samples.

Samples 30 $\mu$ m Layer Thickness	Mean Hardness (HV)	Samples 60 $\mu$ m Layer Thickness	Mean Hardness (HV)	Samples 45 $\mu$ m Layer Thickness	Mean Hardness (HV)
<b>R1</b>	534.37	<b>R5</b>	422.84	<b>R9</b>	514.40
<b>R2</b>	546.43	<b>R6</b>	535.14	<b>R10</b>	523.44
<b>R3</b>	529.33	<b>R7</b>	343.13	<b>R11</b>	535.21
<b>R4</b>	544.20	<b>R8</b>	516.28	-	-
<b>1</b>	539.97	<b>21</b>	462.28	<b>41</b>	523.91
<b>2</b>	570.10	<b>22</b>	545.20	<b>42</b>	553.63
<b>3</b>	535.18	<b>23</b>	345.44	<b>43</b>	495.29
<b>4</b>	552.63	<b>24</b>	528.60	<b>44</b>	538.99
<b>5</b>	533.66	<b>25</b>	358.20	<b>45</b>	451.94
<b>6</b>	546.26	<b>26</b>	535.16	<b>46</b>	534.21
<b>7</b>	490.20	<b>27</b>	150.74	<b>47</b>	345.07
<b>8</b>	532.40	<b>28</b>	461.16	<b>48</b>	492.81
<b>9</b>	526.14	<b>29</b>	463.94	<b>49</b>	525.08
<b>10</b>	564.79	<b>30</b>	546.24	<b>50</b>	557.21
<b>11</b>	530.14	<b>31</b>	342.21	<b>51</b>	513.19
<b>12</b>	549.20	<b>32</b>	529.90	<b>52</b>	543.54
<b>13</b>	525.96	<b>33</b>	339.80	<b>53</b>	487.20
<b>14</b>	538.96	<b>34</b>	536.51	<b>54</b>	534.71
<b>15</b>	480.54	<b>35</b>	155.97	<b>55</b>	313.36
<b>16</b>	529.07	<b>36</b>	460.29	<b>56</b>	527.92
<b>17</b>	449.16	<b>37</b>	462.50	<b>57</b>	527.26
<b>18</b>	528.30	<b>38</b>	472.20	<b>58</b>	512.68
<b>19</b>	534.26	<b>39</b>	470.22	<b>59</b>	528.73
<b>20</b>	531.69	<b>40</b>	529.29	<b>60</b>	535.80

# Appendix – B

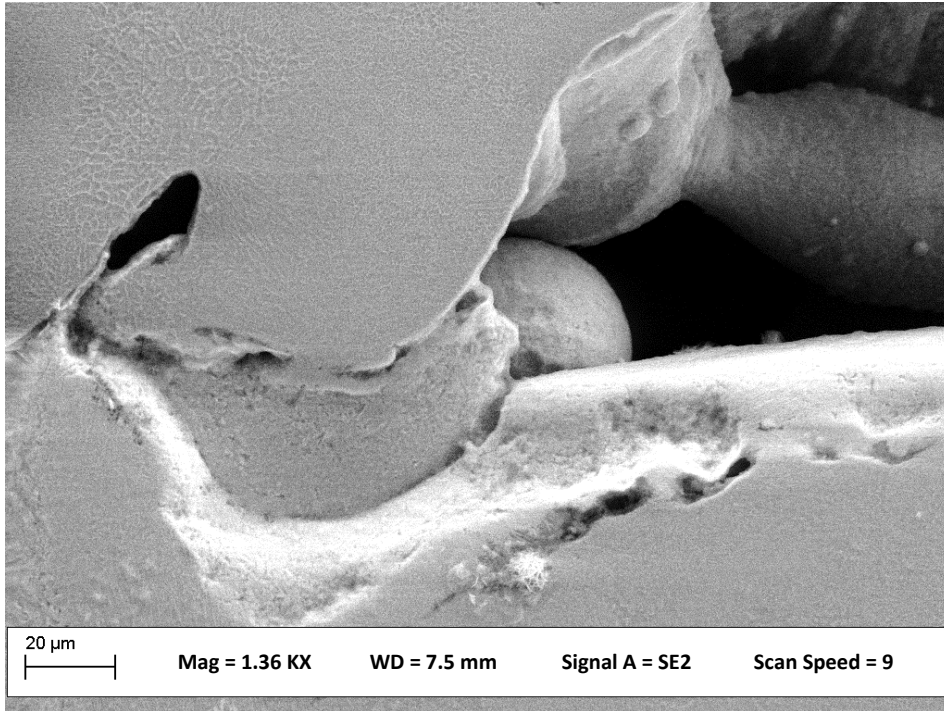


*Fig B-1: None melted powder and lack of fusion for sample R5 (60 μm layer thickness).*

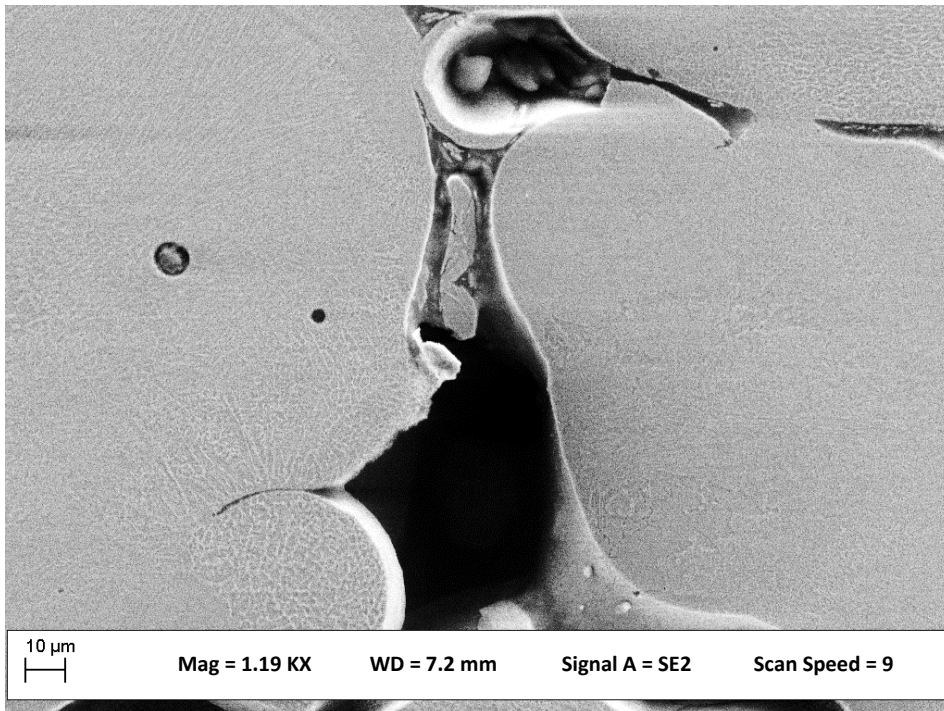


*Fig B-2: Lack of fusion for sample R7 (60 μm layer thickness).*

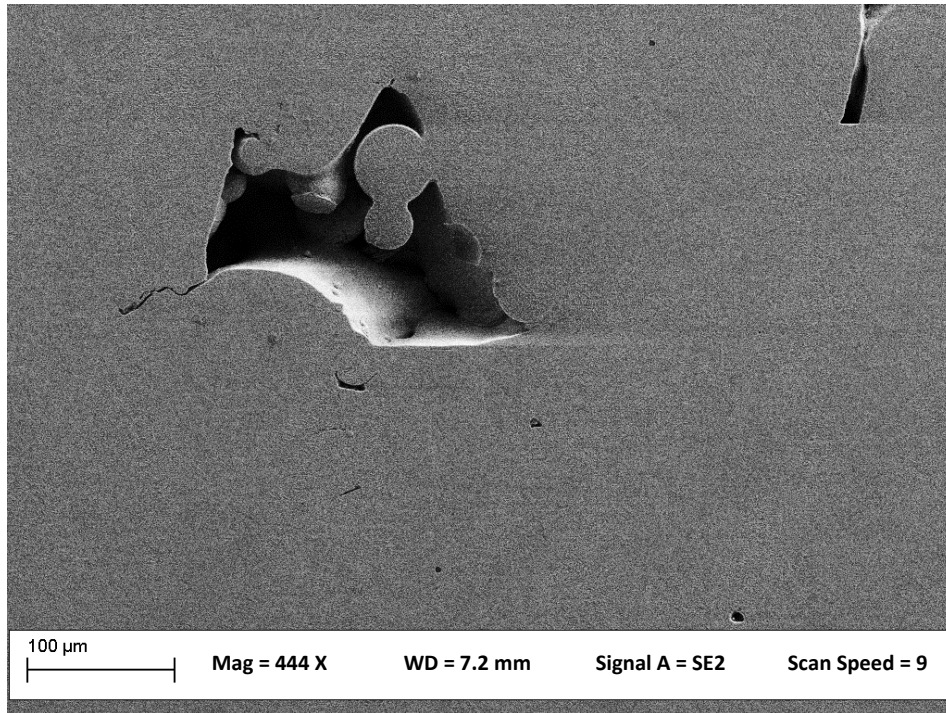


*Fig B-3: Lack of fusion for sample R9 (45 μm layer thickness).*

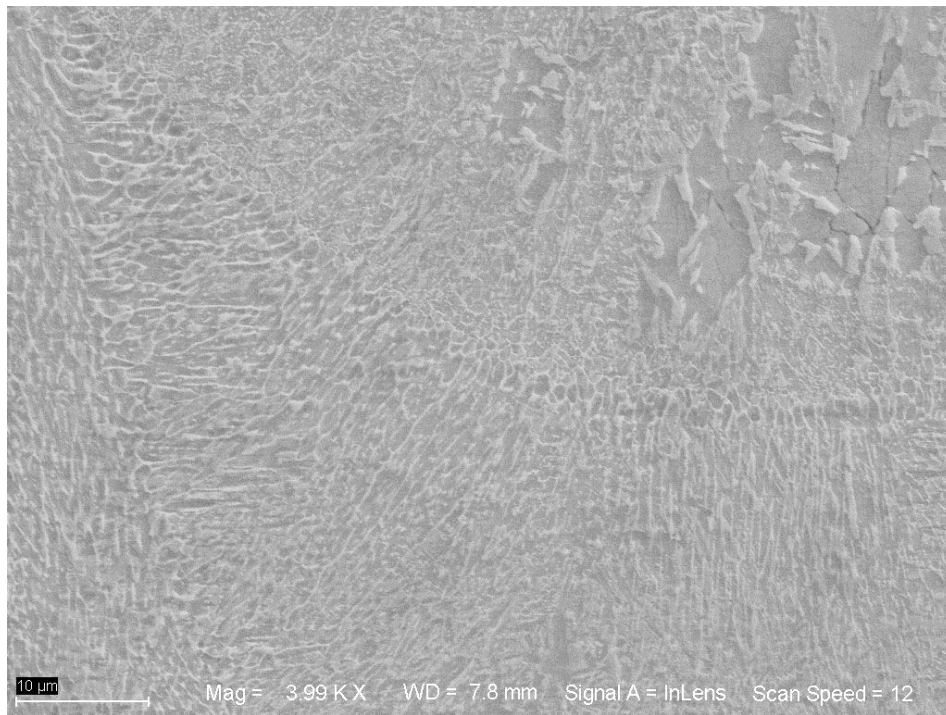


*Fig B-4: defects free microstructure for sample R1 (30 μm layer thickness).*

DEPARTMENT OF INDUSTRIAL AND  
MATERIALS SCIENCE  
CHALMERS UNIVERSITY OF TECHNOLOGY  
Gothenburg, Sweden  
[www.chalmers.se](http://www.chalmers.se)



**CHALMERS**  
UNIVERSITY OF TECHNOLOGY